

Numerical Stability on Local Integral Methods using RBF-QR

L. Ponzellini Marinelli^[1,2]
ponzellini@cifasis-conicet.gov.ar

N. Caruso^[1,2]
caruso@cifasis-conicet.gov.ar

M. Portapila^[1,2]
portapila@cifasis-conicet.gov.ar

- [1] Faculty of Exact Sciences, Engineering and Surveying,
National University of Rosario,
Rosario S2000BTP, Argentina.
- [2] French Argentine International Center
for Information and Systems Sciences,
UAM (France)/UNR-CONICET,
Rosario S2000BTP, Argentina.

November 5, 2018

Abstract

Many local integral methods are based on an integral formulation over small and heavily overlapping stencils with local RBF interpolations. These functions have become an extremely effective tool for interpolation on scattered node sets, however the ill-conditioning of the interpolation matrix -when the RBF shape parameter tends to zero corresponding to best accuracy- is a serious task. Several stabilizing methods have been developed to deal with this near flat RBFs.

The inclusion of the RBF-QR technique in the process of approximating in local integral methods makes possible to avoid this problem and stabilize the numerical error. In this paper we combine this technique in a local integral method and present accuracy results for Poisson, convection-diffusion and thermal boundary layer PDEs.

1 Introduction

The boundary element method (BEM) is now a well-established numerical technique in engineering. The basis of this method is to transform the original partial differential equation (PDE), or system of PDEs that define a given physical problem, into an equivalent integral equation (or system) by means of the corresponding Green's second identity and its fundamental solution, i.e. the Green's integral representation formula. In this way some or all of the field variables and their derivatives are only necessary to be defined at the boundary.

Further increase in the number of applications of the BEM has been hampered by the need to operate with relatively complex fundamental solutions or by the difficulties encountered when these solutions cannot be expressed in a closed form. In the BEM formulation of this kind of problems, it is common to use an integral representation formula based upon a PDE with known closed-form fundamental solution, and express the remaining terms of the original equation as domain integrals. It is known that in these cases the BEM is in disadvantage in comparison with the classical domain schemes, such as the Control Volume (CV) and the Finite Element method (FEM). In the early BEM analysis the evaluation of domain integrals was done using cell integration, a technique which, while effective and general, made the approach too costly computationally due to the successive integration at each cell required for each of the surface collocation points. In order to deal with this, several methods have been developed in the literature to take domain integrals to the boundary in order to eliminate the need for internal cells (boundary-only BEM formulations). One of the most popular methods to date is the dual reciprocity method (DRM) introduced by Nardini and Brebbia [24]. In the DRM, the unknown densities of the corresponding domain integrals are interpolated by a Radial Basis Function (RBF) scheme, and by applying the Green's second identity to a convolution integral of a particular solution and the fundamental solution, the domain integrals are converted

into equivalent surface integrals. However, the DRM approach has the same computational limitations than the cell integration scheme, since very large fully populated matrix systems are obtained. It is important to mention that the DRM approximation is an alternative approach to evaluate domain integrals by defining global domain interpolations and only evaluating surface integrals, but still a domain integration scheme.

When dealing with the BEM for large problems, with or without closed form fundamental solution, it is frequently used a domain decomposition technique, in which the original domain is divided into subdomains, and on each of them the full integral representation formulae are applied. At the interfaces of the adjacent subdomains the corresponding full-matching conditions are imposed (local matrix assembly), as is required in the CV and FEM methods, for which it is necessary to define subdomains or elements connectivity. However, in contrast with the CV and FEM methods, which integral representations of the original PDE are based on weighted residual approximation, in the BEM technique the Green's integral representation formula is an exact representation of the original PDE at each integration subdomain. The BEM matrices for subdomain formulation leads to block banded matrix systems with one block for each subregion and overlaps between blocks when subdomains have a common interface. In the limit of a very large number of subdomains, the resulting internal mesh pattern looks like a finite element grid.

One of these approaches based on large number of subdomains but using the DRM to evaluate the domain integrals at each subdomain, instead of cell integration, has been referred by Popov and Power [28] as the Dual Reciprocity Multi Domain approach (DRM-MD), for more details see Portapila and Power [29]. As previously commented, the most attractive aspect of this type of local BEM approach at the subdomain level is the use of an exact integral representation formula of the original PDE instead of a weighted residual approximation. However, the numerical efficiency of this type of local BEM approaches is still behind of those classical domain numerical schemes. For this reason in recent years significant efforts have been given to the improvement of this type local BEM approaches.

As has been the case in the FEM, see Atluri and Zhu [1], meshless formulations of local BEM approaches, see Zhu et al., [36], are attractive and efficient techniques to improve the performance of local BEM schemes. As in the meshless FEM, in the meshless BEM the integral representation formulae are applied at local internal integration subdomains embedded into

interpolation stencils that are heavily overlapped. In this type of approach the continuity of the field variables are satisfied by the interpolation functions avoiding the local connectivity between subdomains or elements needed to enforce the matching conditions between them. Different interpolation schemes can be employed at the interpolation stencils, being the moving least squares shape functions and RBF interpolations the most popular approaches used in the literature. A major advantage of the meshless local BEM formulations in comparison with the classical BEM multi domain decomposition approaches, as the DRM-MD, is that the resulting integrands of the integral representation formulae are all regular, instead of singular, since the collocation points are always selected inside the integration subdomain.

In the Local Boundary Integral Element Methods (LBEM or LBIEM) the solution domain is covered by a series of small and heavily overlapping local interpolation stencils, where a direct interpolation of the field variables is used to approximate the densities of the integral operator, and the boundary conditions of the problem are imposed at the integral representation formula; i.e. at the global system of equations, resulting in the evaluation of the corresponding weakly and singular surface integrals and if it is the case regular domain integrals, over each of the integration subdomains including those in contact with the problem boundary [36, 35, 34]. In this type of approach, the domains of integration usually are defined over several stencils, resulting in highly overlapping integration subdomains, in addition to the overlapping of interpolation stencils. Both polynomial moving least squares (MLS) approximation and direct RBF interpolations have been previously used in the LBEM as local interpolation algorithms.

In Caruso et. al. [4], the Localized Regular Dual Reciprocity Method (LRDRM) is presented. The LRDRM is an integral domain decomposition method with two distinguishing features, the boundary conditions are imposed at the local interpolation (a local RBF interpolation) level and all the calculated integrals are regular. The "following" work [5] is shown an enhancement of this method where the interpolation functions themselves satisfy the partial differential equation to be solve.

In recent years, the theory of RBFs has undergone intensive research and enjoyed considerable success as a technique for interpolating multivariable functions and for solving PDEs [8, 7, 10]. An RBF $\phi(r)$ depends only on the distance $r = \|\mathbf{x} - \mathbf{x}_k\|$ to a center node \mathbf{x}_k . The methods that use RBFs do not require a grid and it has been shown to be high-order accurate, flexible in nontrivial geometries, computationally efficient and easy to implement.

When infinitely smooth RBFs $\phi(r, \varepsilon)$ are used, the spectral accuracy is often achieved when the shape parameter ε tends to zero. This has been proven for some special cases [21, 3], although numerical experiments suggest that is also true in much general settings. Nevertheless, in practice the interpolation error decreases to low levels until it breaks down due to the numerical ill-conditioning [18, 19], i.e., when $\varepsilon \rightarrow 0$, the RBFs become relatively flat (named *near-flat RBFs*) and the interpolation matrix increases the condition number. This was a -mistaken- trade-off between accuracy and numerical conditioning named as an *uncertainty principle* due to R. Schaback [33] which established that high accuracy and numerical stability cannot arrive simultaneously.

This misconception about the uncertainty principle led to a negative impact on the development for RBFs approximation methods with scattered data. The reason was that the numerical solution denoted as *RBF-Direct* amount to an ill-conditioned numerical procedure for a well-conditioned problem. So, many techniques for stabilizing the error has been developed in the last fifteen year [14, 13, 11, 12]. One of them, the *RBF-QR algorithm* can stably compute interpolants in the case of near-flat RBFs using another basis that generates the same interpolation space.

The RBF-QR technique presented in [11] opened up new possibilities for numerical methods based on local RBF approximations, such as LRDRM since it is possible to stabilize the shape parameter regime for small values of ε .

The following sections in this paper is structured as follows. In Section 2, we describe different formulations of Local Integral Methods with local RBF interpolations. In Section 3 we describe the introduction of the RBF-QR technique into Local Integral approaches. And finally Section 4 contains a variety of numerical examples for Poisson's equations, convection-diffusion and thermal boundary layer equation. Section 5 contains some concluding remarks.

2 Local Integral Methods

2.1 Mathematical formulation and boundary integral representation formulae.

Let us consider the following elliptic problem on a bounded open domain Ω :

$$\begin{cases} \mathcal{L}[u(\mathbf{x})] = f(\mathbf{x}) & \mathbf{x} \in \Omega, \\ \mathcal{B}[u(\mathbf{x})] = g(\mathbf{x}) & \mathbf{x} \in \Gamma = \partial\Omega, \end{cases} \quad (1)$$

where $\mathcal{L}[\cdot]$ is an elliptic operator and $\mathcal{B}[\cdot]$ is a classical boundary operator related with different kind of boundary conditions (e.g. Dirichlet, Neumann or Robin Condition). We assume that the partial differential equation can be rewritten in the following way:

$$\Delta u(\mathbf{x}) = b(\mathbf{x}, u(\mathbf{x}), \nabla u(\mathbf{x})). \quad (2)$$

The integral representation formula for the above PDE in terms of the Laplace's fundamental solution is obtained from the Green's second identity in terms of the superposition of surfaces (single and double layers) and volume potentials is given by

$$c(\xi) u(\xi) = \int_{\Gamma} q^*(\mathbf{x}, \xi) u(\mathbf{x}) d\Gamma_{\mathbf{x}} - \int_{\Gamma} u^*(\mathbf{x}, \xi) q(\mathbf{x}) d\Gamma_{\mathbf{x}} + \int_{\Omega} u^*(\mathbf{x}, \xi) b d\Omega_{\mathbf{x}}, \quad (3)$$

with ξ as the evaluation point, also referred as collocation point, and $u^*(\mathbf{x}, \xi)$ as the fundamental solution of the Laplace problem, which in the case of two-dimensional problems is given by:

$$u^*(\mathbf{x}, \xi) = \frac{1}{2\pi} \ln \left(\frac{1}{R(\mathbf{x}, \xi)} \right), \quad (4)$$

where $R(\mathbf{x}, \xi)$ is the distance between the integration points \mathbf{x} and collocation point ξ , i.e., $R(\mathbf{x}, \xi) = \|\mathbf{x} - \xi\|$, and $q^*(\mathbf{x}) = \frac{\partial u^*}{\partial n}(\mathbf{x}, \xi)$. The constant value $c(\xi) \in [0, 1]$, being 1 if the point ξ is inside the domain and $\frac{1}{2}$ if the point ξ is on a smooth part of the domain boundary Γ (for this work we always will consider $c(\xi) = 1$).

The integral representation formula (3) is the basis of any meshless BEM approach, where the integration surface Γ and domain Ω are chosen as integration subregions, Γ_i and Ω_i , embedded inside of a corresponding interpolation stencils, which are heavily overlapped. Despite of the above formulation,

instead of using the fundamental solution, $u^*(\mathbf{x}, \xi)$, and its normal derivative, $q^*(\mathbf{x}, \xi)$, the Dirichlet Green's Function (DGF), $G(\mathbf{x}, \xi)$ and its corresponding normal derivative, $Q(\mathbf{x}, \xi)$, can be used, it leads that the Eq. (3) at each integration subregion is reduced to:

$$u(\xi) = \int_{\Gamma_i} Q(\mathbf{x}, \xi) u(\mathbf{x}) d\Gamma_{\mathbf{x}} + \int_{\Omega_i} G(\mathbf{x}, \xi) b d\Omega_{\mathbf{x}}, \quad (5)$$

where by definition over the surfaces Γ_i the value of G is identically zero.

In the case a two dimensional problem and a circular subregion of integration Ω_i with radius R_i and centre \mathbf{x}_0 , the Dirichlet Green's Function for a source point, ξ , inside the circle can be obtained from the circle theorem, and given by the Eq. (6) (see Figure 1 for an schematic representation about the elements of the DGF and the details about the circle theorem can be find at [23]):

$$G(\mathbf{x}, \xi) = \begin{cases} \frac{1}{2\pi} \ln \left(\frac{R_i}{R(\mathbf{x}, \xi)} \right) & \text{if } \xi = \mathbf{x}_0, \\ \frac{1}{4\pi} \ln \left(\frac{R_0^2 R(\mathbf{x}, \hat{\xi})^2}{R_i^2 R(\mathbf{x}, \xi)^2} \right) & \text{if } \xi \neq \mathbf{x}_0, \end{cases} \quad (6)$$

with the image or reflection point, $\hat{\xi}$, located outside the circle along the same ray of the source point. In the above expression $R(\mathbf{x}, \xi)$ is the distance between the field point \mathbf{x} and the source point ξ , similarly $R(\mathbf{x}, \hat{\xi})$ is the distance between \mathbf{x} and the image point $\hat{\xi}$ and R_0 is the distance between \mathbf{x}_0 and ξ . In the work [31] there are more details on the features and use of the DGF on the LRDRM.

There are different approaches to evaluate the corresponding volume integrals in (3) and/or (5) in the literature of BEM or Local BEM, one of them consists in approximating the density b of the volume integrals in terms of a interpolation function, i.e.

$$b \approx \sum_{k=1}^N \beta_k \varphi_k(\mathbf{x}) \quad (7)$$

with N as the number of interpolation points and $\varphi_k(\mathbf{x})$ usually is defined

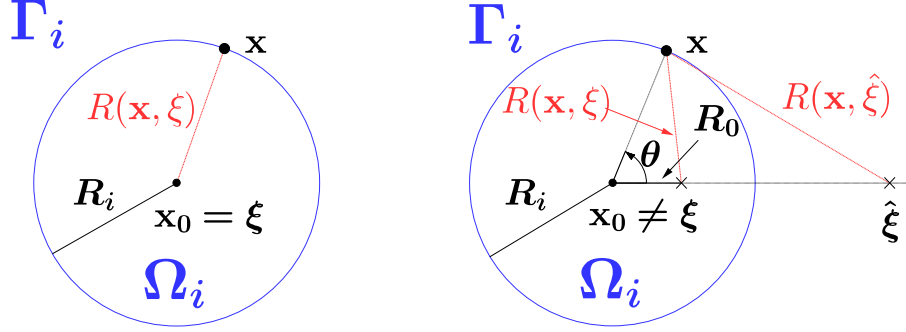


Figure 1: Schematic representation of Dirichlet Green's Function in a circle for centered source $\mathbf{x}_0 = \xi$ (left) and outskirts source point $\mathbf{x}_0 \neq \xi$ (right).

by a RBF. Then the integral representation formulae obtained are:

$$\begin{aligned} u(\xi) &= \int_{\Gamma_i} q^*(\mathbf{x}, \xi) u(\mathbf{x}) d\Gamma_{\mathbf{x}} - \int_{\Gamma_i} u^*(\mathbf{x}, \xi) \frac{\partial u^*}{\partial n}(\mathbf{x}) d\Gamma_{\mathbf{x}} \\ &+ \sum_{k=1}^N \beta_k \int_{\Omega_i} u^*(\mathbf{x}, \xi) \varphi_k(\mathbf{x}) d\Omega_{\mathbf{x}} \end{aligned} \quad (8)$$

or

$$u(\xi) = \int_{\Gamma_i} Q(\mathbf{x}, \xi) u(\mathbf{x}) d\Gamma_{\mathbf{x}} + \sum_{k=1}^N \beta_k \int_{\Omega_i} G(\mathbf{x}, \xi) \varphi_k(\mathbf{x}) d\Omega_{\mathbf{x}}. \quad (9)$$

Futhermore if it is possible find a particular solution $\tilde{\varphi}_k$ such that, $\Delta \tilde{\varphi}_k(\mathbf{x}) = \varphi_k(\mathbf{x})$, then applying again the Green's second identity to the resulting volume integral with the particular solution as density and the fundamental solution as kernel or DGF, the formulae obtained for each subregion are:

$$\begin{aligned} u(\xi) &= \int_{\Gamma_i} q^*(\mathbf{x}, \xi) u(\mathbf{x}) d\Gamma_{\mathbf{x}} - \int_{\Gamma_i} u^*(\mathbf{x}, \xi) \frac{\partial u}{\partial n}(\mathbf{x}) d\Gamma_{\mathbf{x}} \\ &+ \sum_{k=1}^N \beta_k \left\{ \tilde{\varphi}_k(\xi) - \int_{\Gamma_i} q^*(\mathbf{x}, \xi) \tilde{\varphi}_k(\mathbf{x}) d\Gamma_{\mathbf{x}} + \int_{\Gamma_i} \frac{\partial u^*}{\partial n}(\mathbf{x}, \xi) \tilde{\varphi}_k(\mathbf{x}) d\Gamma_{\mathbf{x}} \right\} \end{aligned}$$

or

$$u(\xi) = \int_{\Gamma_i} Q(\mathbf{x}, \xi) u(\mathbf{x}) d\Gamma_{\mathbf{x}} + \sum_{k=1}^N \beta_k \left\{ \tilde{\varphi}_k(\xi) - \int_{\Gamma_i} Q(\mathbf{x}, \xi) \tilde{\varphi}_k(\mathbf{x}) d\Gamma_{\mathbf{x}} \right\}. \quad (11)$$

2.2 Local Integral approaches I: Localized Regular Dual Reciprocity Method (LRDRM)

In the local meshless BEM approaches the integral representation formulae are applied at local internal subdomain or subregion (as Ω_i and Ω_j in the Figure 2) embedded into interpolation stencils that are heavily overlapped (as Θ_i and Θ_j in the Figure 2).

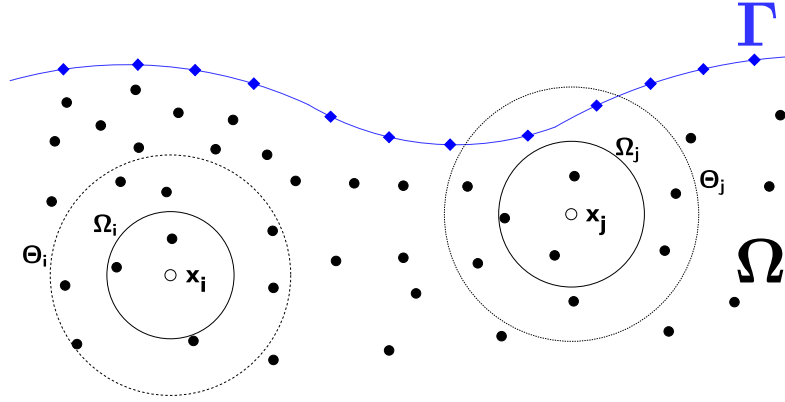


Figure 2: Schematic representation of local stencils Θ_i and local subdomains or subregions Ω_i for different local meshless BEM

In this article we consider the approach presented in Caruso et al. [4] and Power et al. [31], i.e. the LRDRM, the computational domain is covered by a set of integration subregions (where the integral representation formula is applied) and a set of heavily overlapping interpolation stencils with the important features; the first one, the boundary conditions of the problem are imposed locally at the interpolation stencil; and the second one, the collocation point (where the Delta function is centered) is always inside the subregion in order to obtain that every boundary integral in the local integral approach is regular.

Then the field variable $u(\mathbf{x})$ is approximated by a RBF interpolation using the corresponding nodes of the interpolation stencil, plus some additional auxiliary boundary points (if the stencil is next to the global boundary). The set $\{(\mathbf{x}_j, u(\mathbf{x}_j))\}_{j=1}^{n_i}$ is formed by the internal nodes \mathbf{x}_j and the corresponding unknown nodal values $u(\mathbf{x}_j)$ for $j = 1, \dots, n_i$. The other set $\{(\mathbf{x}_j, \mathcal{B}(u(\mathbf{x}_j)))\}_{j=n_i+1}^{n_i+n_b}$ has the boundary nodes \mathbf{x}_j and the boundary

data $\mathcal{B}(u(\mathbf{x}_j))$ for $j = n_i + 1, \dots, n_i + n_b$. Then the local approximation is presented as

$$u(\mathbf{x}) = \sum_{j=1}^n \alpha_j \varphi_j(\mathbf{x}) \quad (12)$$

being $\varphi_j(\mathbf{x}) = \phi(\|\mathbf{x} - \mathbf{x}_j\|)$ the RBFs interpolating functions and $n = n_i + n_b$ where n_i is the number of internal points of the stencil and n_b is the number of auxiliary points given by the boundary points belonging to an interpolation stencil next to the problem boundary. In this way, at interpolation stencils inside the problem domain $n_b = 0$, and at those in contact with the problem boundary, n_b is equal to the number of boundary collocation points belonging to the given stencil.

Different RBFs have been considered as local interpolating functions in integral methods. In [4] were used the MQ1, MQ2 and TPS. Other important and well established RBF are the Gaussians that depends on a shape parameter ε . All these RBFs corresponds to the two main groups of RBFs: piecewise smooth and infinitely smooth. Some examples are given in Table 1. For these examples and many others, it had been demonstrated that the linear system of equations formed in the local interpolation is non-singular, in any dimension and for any number of nodes. This set of nodes must be different and *unisolvant*. For more details, see [8, 10].

Infinitely smooth RBFs	$\phi(r, \varepsilon)$	Polynomial
Gaussian (GA)	$e^{-(\varepsilon r)^2}$	no poly
Multiquadric 1 (MQ1)	$\sqrt{1 + (\varepsilon r)^2}$	$p(x) \in \mathbb{P}_0(x)$
Multiquadric 2 (MQ2)	$(1 + (\varepsilon r)^2)^{\frac{3}{2}}$	$p(x) \in \mathbb{P}_1(x)$
Piecewise smooth RBFs	$\phi(r)$	Polynomial
Thin Plate Spline (TPS)	$r^4 \log(r)$	$p(x) \in \mathbb{P}_2(x)$

Table 1: Piecewise (TPS) and infinitely smooth (GA, MQ1, MQ2) RBFs with the corresponding polynomials to ensure non-singularity of the interpolation matrix used in this work. $r = \|\mathbf{x} - \mathbf{x}_j\|$ denotes the distance to the centre of the RBF and ε the shape parameter.

By using this interpolation scheme, the value of the unknown u in (12), over an integration subregion is obtained from the interpolation reconstruction formula as:

$$u(\mathbf{x}) = \boldsymbol{\varphi}(\mathbf{x})^T \mathbf{A}^{-1} \mathbf{d}, \quad (13)$$

with \mathbf{A}^{-1} as the corresponding inverse interpolation matrix; and the vector \mathbf{d} in terms of the unknown nodal values $\mathbf{u} = [u_1, \dots, u_{n_i}]$ and the prescribed boundary condition values $g(\mathbf{u}_b) = [g(\mathbf{x}_{n_i+1}), \dots, g(\mathbf{x}_n)]$ with g from Eq. (1) (i.e., $\mathbf{d} = \mathbf{u}^T$ for internal stencils and $\mathbf{d} = [\mathbf{u}, g(\mathbf{u}_b)]^T$ for boundary stencils). After inversion of the interpolation matrix A , the interpolation coefficients are given by:

$$\alpha = \mathbf{A}^{-1}\mathbf{d}. \quad (14)$$

In cases where the non-homogeneous term b in (2) is function of the derivative of the field variable u , we use the generalized finite different approximation where this value is approximated by the derivative of the interpolation reconstruction function in terms of the neighbouring values of u at the interpolation stencils, i.e.,

$$\frac{\partial u(\mathbf{x})}{\partial x_i} = \frac{\partial \varphi(\mathbf{x})^T}{\partial x_i} \mathbf{A}^{-1}\mathbf{d}. \quad (15)$$

Substituting (12) into the integral formula (11) with $\xi = \mathbf{x}_i$ a trial point inside Ω_i , the integration subregion, the discretized form for the unknown $u_i = u(\mathbf{x}_i)$ reduces to:

$$u_i = \sum_{j=1}^n \alpha_j h_{ij} + \sum_{j=1}^n \beta_j \tilde{h}_{ij}, \quad (16)$$

or in matrix notation:

$$u_i = \mathbf{h}_i^T \alpha + \tilde{\mathbf{h}}_i^T \beta, \quad (17)$$

where

$$h_{ij} = \int_{\Gamma_i} Q(\mathbf{x}, \mathbf{x}_i) \varphi_j(\mathbf{x}) d\Gamma_{\mathbf{x}} \quad (18)$$

$$\tilde{h}_{ij} = \tilde{\varphi}_j(\mathbf{x}_i) - \int_{\Gamma_i} Q(\mathbf{x}, \mathbf{x}_i) \tilde{\varphi}_j(\mathbf{x}) d\Gamma_{\mathbf{x}} \quad (19)$$

with the column vectors $\mathbf{h}_i = [\dots, h_{ij}, \dots]^T$ and $\tilde{\mathbf{h}}_i = [\dots, \tilde{h}_{ij}, \dots]^T$.

All the integrals in the above formulations are regulars, since the collocation points are located inside the integration subregion, and they are

evaluated through the Gauss-Legendre quadrature. Also notice that the interpolation coefficients α and β in equation (17) correspond to the interpolation of the field variable and the non-homogeneous part of the PDE, respectively, both of them given in terms of the stencil nodal values of the field variable.

When possible, in the DRM interpolation it is considered that

$$b(\mathbf{x}, u(\mathbf{x}), \nabla u(\mathbf{x})) = f(\mathbf{x}) + \tilde{b}(u(\mathbf{x}), \nabla u(\mathbf{x})) \approx \sum_{j=1}^n \beta_j \varphi_j(\mathbf{x}) \quad (20)$$

similarly to equation (14) beta is written as: $\beta = \tilde{\mathbf{A}}^{-1}(\mathbf{f}_i + \tilde{\mathbf{b}}_i)$, where the vector \mathbf{f}_i is given by a data function evaluation and $\tilde{\mathbf{b}}_i$ can be written as a function of \mathbf{d} (i.e. in terms of the nodal values in \mathbf{u} and boundary conditions values $g(\mathbf{u}_b)$), from the following expression for $\tilde{b}(u(\mathbf{x}), \nabla u(\mathbf{x}))$ and its linearity:

$$\tilde{b}(u(\mathbf{x}), \nabla u(\mathbf{x})) = \tilde{b}(\varphi_j(\mathbf{x}), \nabla \varphi_j(\mathbf{x})) \mathbf{A}^{-1} \mathbf{d}, \quad (21)$$

therefore

$$\beta = \tilde{\mathbf{A}}^{-1} (\mathbf{f}_i + \mathbf{A}_b \mathbf{A}^{-1} \mathbf{d}) \quad (22)$$

with matrix coefficients $(\mathbf{A}_b)_{kj} = \tilde{b}(\varphi_j(\mathbf{x}_k), \nabla \varphi_j(\mathbf{x}_k))$.

In the above expression the matrices \mathbf{A} and $\tilde{\mathbf{A}}$ are identical at stencils in the interior of the problem domain, however, at boundary stencils the matrix \mathbf{A} is defined by the corresponding interpolation matrix according to the boundary conditions of the problem, while the matrix $\tilde{\mathbf{A}}$ is the same direct interpolation matrix. We note \mathbf{A}_b as the matrix corresponding to calculus of the vector $\tilde{\mathbf{b}}_i$.

Equation (17) can be written in terms of \mathbf{d} by substituting into it the expression (14), resulting the following equation:

$$u_i = \tilde{\mathbf{h}}_i^T \tilde{\mathbf{A}}^{-1} \mathbf{f}_i + \left(\mathbf{h}_i^T \mathbf{A}^{-1} + \tilde{\mathbf{h}}_i^T \tilde{\mathbf{A}}^{-1} \mathbf{A}_b \mathbf{A}^{-1} \right) \mathbf{d}. \quad (23)$$

Finally equation (23) is collocated at each trial point of each stencil to form a global sparse matrix system. This equation is obtained in a way that is possibly to avoid calculating numerically the inverse matrix \mathbf{A}^{-1} and $\tilde{\mathbf{A}}^{-1}$. This method is called in the rest of this work as the *Localized Regular Dual Reciprocity Method (LRDRM)*.

2.3 Local Integral approaches II: Local Integral Method (LIM)

The main aim in the using of DRM in a global integral method as BEM is try to avoid the cost of numerical calculus of domain integrals, because in this kind of method with N degrees of freedom it is necessary N^2 of operations whereas for boundary integrals is N , but in local method with a local n (a fix low number) degrees of freedom it does not seem a big deal.

From Eq. (20) the non-homogeneous term was splitted up in a known data function f plus a linear unknown term \tilde{b} , so in order to get more accuracy, the data function f is integrated directly (with the corresponding DGF) instead of approximated it

$$u(\xi) = \int_{\Gamma_i} Q(\mathbf{x}, \xi) u(\mathbf{x}) d\Gamma_i + \int_{\Omega_i} f(\mathbf{x}) Q(\mathbf{x}, \xi) d\Omega_i + \int_{\Omega_i} \tilde{b}(u, \nabla u) Q(\mathbf{x}, \xi) d\Omega_i \quad (24)$$

where the linear term \tilde{b} is locally interpolated with RBFs.

Then from the local approach in the above equation and using the same local RBF interpolation scheme Θ_i we can obtain the following equation:

$$u_i = \sum_{j=1}^n \alpha_j h_{ij} + \sum_{j=1}^n \beta_j \tilde{h}_{ij} + f_i, \quad (25)$$

where α_j, β_j and h_{ij} are calculated as in Eq. (16) and

$$\begin{aligned} \tilde{h}_{ij} &= \int_{\Omega_i} G(\mathbf{x}, \mathbf{x}_i) \varphi_j(\mathbf{x}) d\Omega_{\mathbf{x}}, \\ f_i &= \int_{\Omega_i} G(\mathbf{x}, \mathbf{x}_i) f(\mathbf{x}) d\Omega_{\mathbf{x}}. \end{aligned} \quad (26)$$

The obtained the equation is

$$u_i = f_i + \left(\mathbf{h}_i^T \mathbf{A}^{-1} + \tilde{\mathbf{h}}_i^T \tilde{\mathbf{A}}^{-1} \mathbf{A}_b \mathbf{A}^{-1} \right) \mathbf{d} \quad (27)$$

which is collocated at each trial point of each stencil to form a global sparse matrix system.

As before, to avoid calculating numerically the inverse matrix \mathbf{A}^{-1} and $\tilde{\mathbf{A}}^{-1}$ we rewrite this expression as

$$u_i = f_i + \mathbf{z}_i^T \mathbf{d} \quad (28)$$

where the algorithmic procedure to calculate this equation is the following:

Step 1. Solve $\tilde{\mathbf{A}} \tilde{\mathbf{w}}_i = \tilde{\mathbf{h}}_i$ (since $\tilde{\mathbf{A}}$ simetric).

Step 2. $\mathbf{w}_i^T = \mathbf{h}_i^T + \tilde{\mathbf{w}}_i^T \mathbf{A}_b$.

Step 3. Solve $\mathbf{A}^T \mathbf{z}_i = \mathbf{w}_i$.

In Steps 1 and 3 the ill-conditioning of the linear systems could significant. We call this method *Local Integral Method (LIM)*.

All these equations are ensamble resulting a sparse linear system. In this paper we used an iterative solver, as the restarted GMRES method that has computational cost of the order $O(\gamma N^\beta N n)$ with γ and β depending on the structure of the matrix and numerical scheme employed (for detail about the computational cost of the GMRES scheme used in this work see Guttel and Pestana [16]).

3 Introducing RBF-QR into a Local Integral Method

3.1 The Local Integral RBF-QR Method

In this section, we introduce the RBF-QR method presented in [13, 11, 20] into the local RBF interpolations for the Local Integral Methods developed in Section 2 to get a new formulae for local meshless methods. The principal porpouse is to bypass the ill-conditioning of the RBF-Direct approach (present in the LRDRM) for near-flat RBFs.

As it is explain later we change the Dual Reciprocity formulation to introduce the RBF-QR to get a new formulation called *Local Integral RBF-QR Method (LIM RBF-QR)*.

From Eq. (12), the unknown u field is interpolated locally at each stencil Θ_i with RBF interpolating functions $\varphi_j(\mathbf{x}, \varepsilon) = \phi(\|\mathbf{x} - \mathbf{x}_j\|, \varepsilon)$ that depends on a shape parameter $\varepsilon > 0$ where $\xi_j \in \Theta_i$ the collocation point and $\mathbf{x}_j \in \Theta_i$ for $j = 1, \dots, n_i + n_b$. See Fig. 6.

If there is no boundary node in Θ_i (as the interior stencil in that Figure), the interpolation matrix of the linear system for the local approximation (12) takes the form

$$\mathbf{A} = \begin{bmatrix} \phi(\|\mathbf{x}_1 - \mathbf{x}_1\|, \varepsilon) & \phi(\|\mathbf{x}_1 - \mathbf{x}_2\|, \varepsilon) & \dots & \phi(\|\mathbf{x}_1 - \mathbf{x}_{n_i}\|, \varepsilon) \\ \phi(\|\mathbf{x}_2 - \mathbf{x}_1\|, \varepsilon) & \phi(\|\mathbf{x}_2 - \mathbf{x}_2\|, \varepsilon) & \dots & \phi(\|\mathbf{x}_2 - \mathbf{x}_{n_i}\|, \varepsilon) \\ \vdots & \vdots & \ddots & \vdots \\ \phi(\|\mathbf{x}_{n_i} - \mathbf{x}_1\|, \varepsilon) & \phi(\|\mathbf{x}_{n_i} - \mathbf{x}_2\|, \varepsilon) & \dots & \phi(\|\mathbf{x}_{n_i} - \mathbf{x}_{n_i}\|, \varepsilon) \end{bmatrix}. \quad (29)$$

As it is known, the RBFs constitute an ill-conditioned basis in a good approximation space. When the shape parameter ε tends to zero, the interpolation error often decreases to low levels until it break downs [18, 33] when solving the linear system of the interpolation with a direct method. This is because the interpolation matrix (29) becomes increasingly ill-conditioned and the expansion coefficients α_j in (12) becomes large magnitude and oscillatory causing numerical cancellations when using the reconstruction formula in (7) and (12).

The Fig. 3 shows the cases for Gaussians RBFs, $\varphi(r, \varepsilon) = e^{-(r\varepsilon)^2}$ for different ε s. For small and fixed shape parameter, the distance matrix of the RBF makes flatter (called near flat RBFs), so the linear combination of these kind of RBFs for interpolation becomes almost linear dependant like the case $\varepsilon = 0.1$ in the Fig. 3.

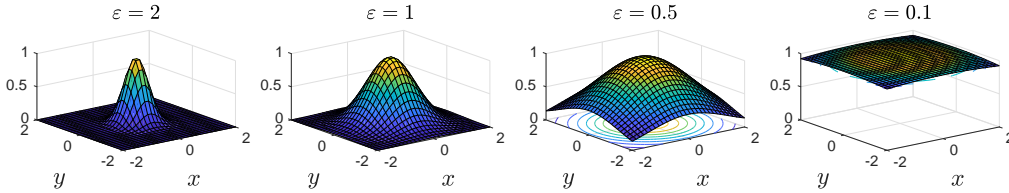


Figure 3: RBF GA when $\varepsilon = 2, 1, 0.1$.

To avoid the ill-conditioning presented in the local interpolation of u and also in the interpolation of the density term b , we change the basis as it was developed in the RBF-QR method in 2-dimensions [11]. The new expansion

of the Gaussian RBF takes the form:

$$\phi(\|\mathbf{x} - \mathbf{x}_j\|) = \sum_{k=0}^{\infty} \sum_{l=0}^{\lfloor k/2 \rfloor} d_{k,l} c_{k,j}(\mathbf{x}_j) C_{k,l}(\mathbf{x}) \quad (30)$$

$$+ \sum_{k=0}^{\infty} \sum_{l=1-p}^{\lfloor k/2 \rfloor} d_{k,l} s_{k,l}(\mathbf{x}_j) S_{k,l}(\mathbf{x}), \quad (31)$$

where $p = 0$ if k even and $p = 1$ if k odd. The scale factors $d_{k,l}$ is $O(\varepsilon^{2k})$ are

$$d_{k,l} = \frac{\varepsilon^{2k}}{2^{k-2l-1} \left(\frac{k+2l+p}{2}\right)! \left(\frac{k-2l-p}{2}\right)!}, \quad (32)$$

and the coefficients $c_{k,l}, s_{k,l}$ are $O(1)$ given by

$$c_{k,l}(\mathbf{x}_j) = b_{2l+p} t_{k-2l} e^{-\varepsilon^2 r_j^2} \cos((2l+p)\theta_j) {}_1F_2(\alpha_{k,l}, \beta_{k,l}, \varepsilon^4 r_j^2), \quad (33)$$

$$s_{k,l}(\mathbf{x}_j) = b_{2l+p} t_{k-2l} e^{-\varepsilon^2 r_j^2} \sin((2l+p)\theta_j) {}_1F_2(\alpha_{k,l}, \beta_{k,l}, \varepsilon^4 r_j^2), \quad (34)$$

where $b_0 = 1$, $b_k = 2, \forall k > 0$, $t_0 = 1/2$, $t_k = 1, \forall k > 0$, ${}_1F_2$ is the hypergeometric function with parameters $\alpha = \frac{k-2l+p+1}{2}$ and $\beta = [k-2l+1, \frac{k+2l+p+2}{2}]$ being (r_j, θ_j) is the polar coordinates location of the node \mathbf{x}_j .

The expansion functions $C_{k,l}$ and $S_{k,l}$ in (30) and (31) are given by

$$C_{k,l}(\mathbf{x}) = e^{-\varepsilon^2 r^2} r^{2l} T_{k-2l}(r) \cos((2l+p)\theta), \quad (35)$$

$$S_{k,l}(\mathbf{x}) = e^{-\varepsilon^2 r^2} r^{2l} T_{k-2l}(r) \sin((2l+p)\theta), \quad 2l+p \neq 0 \quad (36)$$

where $\{T_n(r)\}$ are the Chebyshev polynomials.

Fig. 4 shows the four level of expansion functions used to generated $C_{k,l}(\mathbf{x})$ and $S_{k,l}(\mathbf{x})$ for small shape parameter $\varepsilon = 0.1$ wich seems to be clearly linear independant. As $\varepsilon \rightarrow 0$, the term $e^{-\varepsilon^2 r^2} \rightarrow 1$ and the basis tends to the basis $\{1, r, r^r, r^3, \dots\}$ which is again an ill-conditioned basis because high powers of r tend to be nearly dependent. The introduction of the Chebyshev polynomials in Eqs. (35) and (36) instead of monomials improve this situation. For more details see [11].

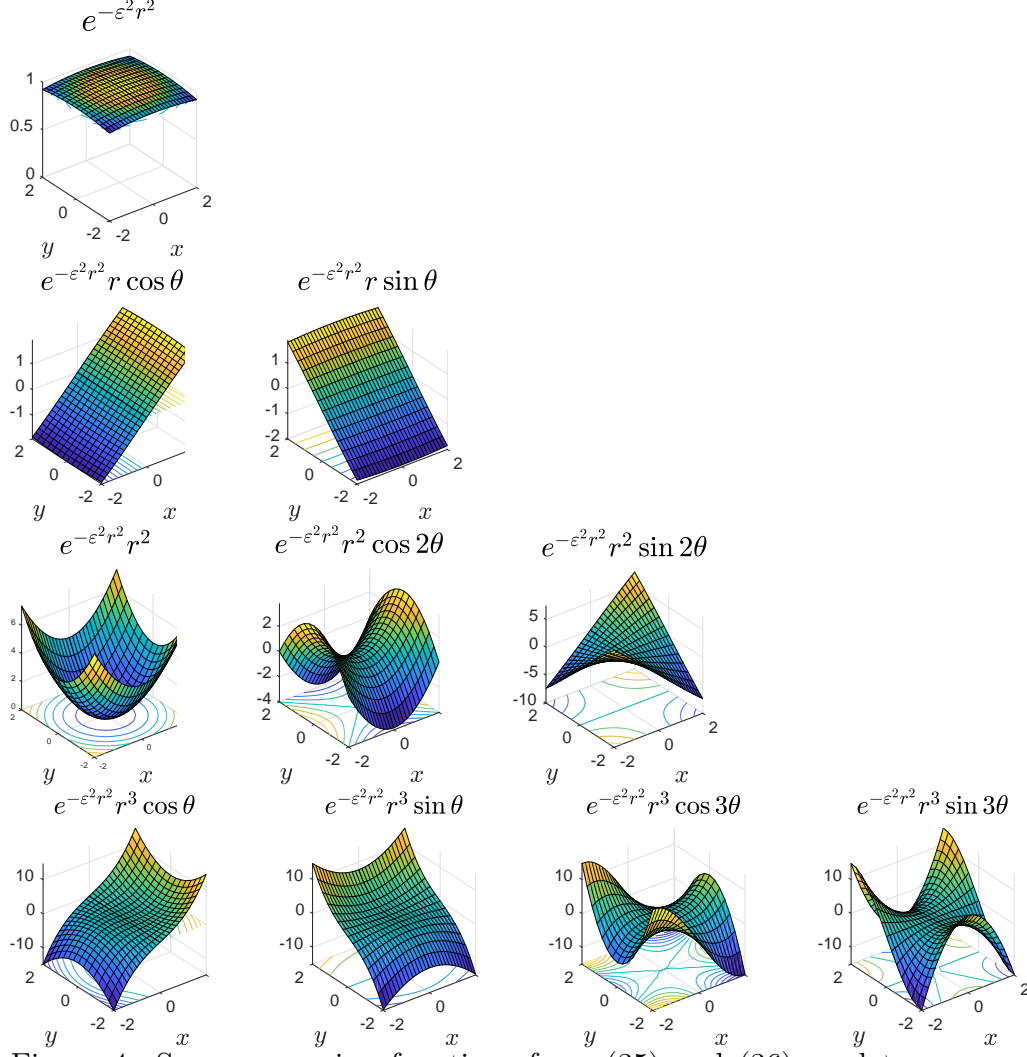


Figure 4: Some expansion functions from (35) and (36) used to represent RBF GA for $\epsilon = 0.1$.

In matrix form, each Gaussian RBF basis has the infinitely expansion

$$\begin{bmatrix} \varphi_1(\mathbf{x}) \\ \varphi_2(\mathbf{x}) \\ \vdots \\ \varphi_n(\mathbf{x}) \end{bmatrix} = \begin{bmatrix} \cdot & \cdot & \cdots \\ \cdot & c_{k,l} & \cdots \\ \cdot & s_{k,l} & \cdots \\ \cdot & \cdot & \cdots \end{bmatrix} \begin{bmatrix} \ddots & & & \\ & d_{k,l} & & \\ & & \ddots & \\ & & & \ddots \end{bmatrix} \begin{bmatrix} C_{0,0}(\mathbf{x}) \\ C_{1,0}(\mathbf{x}) \\ S_{1,0}(\mathbf{x}) \\ C_{2,0}(\mathbf{x}) \\ C_{2,1}(\mathbf{x}) \\ S_{2,1}(\mathbf{x}) \\ \vdots \end{bmatrix}. \quad (37)$$

If we rename the functions $C_{k,l}$ and $S_{k,l}$ as V_k , the coefficients $c_{k,l}$ and $s_{j,m}$ as \tilde{c}_k , $d_{j,m}$ as \tilde{d}_k and truncating for some m , we get the new basis approximation in matrix form

$$\begin{bmatrix} \varphi_1(\mathbf{x}) \\ \varphi_2(\mathbf{x}) \\ \vdots \\ \varphi_n(\mathbf{x}) \end{bmatrix} \approx \begin{bmatrix} \tilde{c}_1(\mathbf{x}_1) & \dots & \tilde{c}_m(\mathbf{x}_1) \\ \vdots & \ddots & \vdots \\ \tilde{c}_1(\mathbf{x}_n) & \dots & \tilde{c}_m(\mathbf{x}_n) \end{bmatrix} \begin{bmatrix} \tilde{d}_1 & & \\ & \ddots & \\ & & \tilde{d}_m \end{bmatrix} \begin{bmatrix} V_1(\mathbf{x}) \\ \vdots \\ V_m(\mathbf{x}) \end{bmatrix}. \quad (38)$$

QR-factorizing the matrix \mathbf{C} , we obtain

$$\begin{bmatrix} \varphi_1(\mathbf{x}) \\ \varphi_2(\mathbf{x}) \\ \vdots \\ \varphi_n(\mathbf{x}) \end{bmatrix} \approx \mathbf{C} \mathbf{D} \begin{bmatrix} V_1(\mathbf{x}) \\ V_2(\mathbf{x}) \\ \vdots \\ V_m(\mathbf{x}) \end{bmatrix} = (\mathbf{Q}\mathbf{R})\mathbf{D} \mathbf{V}(\mathbf{x}) \quad (39)$$

$$= \mathbf{Q} [\mathbf{R}_1 \mathbf{D}_1 \mid \mathbf{R}_2 \mathbf{D}_2] \mathbf{V}(\mathbf{x}) \quad (40)$$

where \mathbf{C} is a $n \times m$ rectangular matrix where the elements of the coefficients are $O(1)$, \mathbf{D} is a $m \times m$ diagonal matrix with the scaling coefficients \tilde{d}_k proportional to ε^{2k} for the integer $k \geq 0$, \mathbf{Q} the $n \times n$ orthonormal matrix and \mathbf{R} the $n \times n$ upper-triangular from QR algorithm.

The matrix \mathbf{R} is partitioned as $[\mathbf{R}_1 \mid \mathbf{R}_2]$ where \mathbf{R}_1 the upper triangular that contains the n first columns of \mathbf{R} and \mathbf{R}_2 is a matrix block $n \times m$. The scaling matrix \mathbf{D} is partitioned correspondingly with \mathbf{D}_1 a $n \times n$ diagonal block and \mathbf{R}_2 of size $(m - n) \times (m - n)$.

The vector function $\mathbf{V}(\mathbf{x})$ has components the functions $V_k(\mathbf{x})$ combination of monomials, Chebyshev polynomials and trigonometric functions.

The new basis $\{\psi_j(\mathbf{x})\}$ is given by:

$$\begin{bmatrix} \psi_1(\mathbf{x}) \\ \psi_2(\mathbf{x}) \\ \vdots \\ \psi_n(\mathbf{x}) \end{bmatrix} = \mathbf{D}_1^{-1} \mathbf{R}_1^{-1} \mathbf{Q}^T \begin{bmatrix} \varphi_1(\mathbf{x}) \\ \varphi_2(\mathbf{x}) \\ \vdots \\ \varphi_n(\mathbf{x}) \end{bmatrix} \approx [\mathbf{I}_n \mid \tilde{\mathbf{R}}] \mathbf{V}(\mathbf{x}) \quad (41)$$

with \mathbf{I}_n the identity matrix of size $n \times n$ and $\tilde{\mathbf{R}} = \mathbf{D}_1^{-1} \mathbf{R}_1^{-1} \mathbf{R}_2 \mathbf{D}_2$ the correction matrix that contains nonnegative powers of ε due to the ordering of the scaling coefficients that generate local interpolation matrices better conditioned.

Now, for introducing the RBF-QR method into the integral formulations presented in Section 2, the field variable u is calculated numerically in the new basis over each integral subregions Ω_i and its corresponding boundary $\partial\Omega_i$,

$$u(\mathbf{x}) = \sum_{k=1}^n \gamma_k \psi_k(\mathbf{x}) \quad (42)$$

where the new coefficients $\{\gamma_k\}_{k=1}^n$ are to be determined. Also the non-homogeneous term b is interpolated in the new basis as in Eq. (7)

$$b \approx \sum_{k=1}^n \lambda_k \psi_k(\mathbf{x}) \quad (43)$$

with the new coefficients $\{\lambda_k\}_{k=1}^n$ to be determined.

In the same way that in the integral method presented above, we have an interpolation matrix for u (denoted as \mathbf{B}) and another for b (denoted as $\tilde{\mathbf{B}}$). These matrices can be obtained using the new basis.

For the internal stencils it is well known that they are equals and can be computed in a direct way, $(\mathbf{B})_{ik} = \psi_k(\mathbf{x}_i)$ for $i, k = 1, \dots, n$, applying the transpose relation to Eq. (41) at each center node \mathbf{x}_i to get the new matrix

$$\mathbf{B}_\psi = \mathbf{V} \begin{bmatrix} \mathbf{I}_n \\ \tilde{\mathbf{R}}^T \end{bmatrix}. \quad (44)$$

where the matrix \mathbf{V} has elements $v_{ik} = V_k(\mathbf{x}_i)$.

It is well known that for positive definite Gaussians RBFs the interpolation matrix is always nonsingular for distinct nodes and $\varepsilon > 0$ as was demonstrated by C.A. Micchelli in [22]. In this case the matrix \mathbf{B}_ψ is nonsingular since the change of basis is well defined Eq. (41) and as it was also discussed in [20].

When we have Neumann boundary conditions, we need to calculate the partial derivative $\frac{\partial \psi_k}{\partial n}(\mathbf{x})$ at some nodes $\{\mathbf{x}_i\}_{i=n_i+1}^n$ of the new basis functions. For this, we need to observe that functions $\{\psi_k\}$ depend linearly on the expansion functions $\{V_k\}$. So, from Eq. (41) it is possible to calculate numerically the action of a boundary linear operator \mathcal{B} on this basis as

$$\begin{bmatrix} \mathcal{B}\psi_1(\mathbf{x}) \\ \mathcal{B}\psi_2(\mathbf{x}) \\ \vdots \\ \mathcal{B}\psi_n(\mathbf{x}) \end{bmatrix} \approx \begin{bmatrix} \mathbf{I}_n & \tilde{\mathbf{R}} \end{bmatrix} \begin{bmatrix} \mathcal{B}V_1(\mathbf{x}) \\ \mathcal{B}V_2(\mathbf{x}) \\ \vdots \\ \mathcal{B}V_m(\mathbf{x}) \end{bmatrix} = \begin{bmatrix} \mathbf{I}_n & \tilde{\mathbf{R}} \end{bmatrix} \mathbf{W}(\mathbf{x}). \quad (45)$$

where the vector function $\mathbf{W}(\mathbf{x})$ has components $\mathcal{B}V_k(\mathbf{x})$, $k = 1, \dots, m$.

So, the local matrix interpolation \mathbf{B} that arises for the boundary stencil is formed with matrix blocks

$$\mathbf{B} = \begin{bmatrix} \mathbf{B}_\psi \\ \mathbf{B}_{\mathcal{B}\psi} \end{bmatrix}. \quad (46)$$

where the block \mathbf{B}_ψ has coefficients $(\mathbf{B}_\psi)_{ik} = \psi_k(\mathbf{x}_i)$ for $i = 1, \dots, n_i$ and $k = 1, \dots, n$ and the other block $\mathbf{B}_{\mathcal{B}\psi}$ has coefficients $(\mathbf{B}_{\mathcal{B}\psi})_{ik} = \mathcal{B}\psi_k(\mathbf{x}_i)$ for $i = n_i + 1, \dots, n$ and $k = 1, \dots, n$. The Matlab's implementation used for calculating these matrix blocks is the algorithm `RBF_QR_diffmat_2D` available from the first author's website in [20].

As in Eq. (14) and (22), the new local interpolation coefficients are now given by:

$$\lambda = \mathbf{B}^{-1} \mathbf{d} \quad (47)$$

and

$$\beta = \tilde{\mathbf{B}}^{-1} (\mathbf{f}_i + \mathbf{B}_b \mathbf{B}^{-1} \mathbf{d}) \quad (48)$$

with matrix coefficients $(\mathbf{B}_b)_{kj} = \tilde{b}(\psi_j(\mathbf{x}_k), \nabla \psi_j(\mathbf{x}_k))$.

So taking $\xi = \xi_i$ as in the local approach in Eq. (9) for each interior collocation point $\{\xi_i\}$, we have

$$u_i = \sum_{k=1}^n l_{ik} \gamma_k + \sum_{k=1}^n \tilde{l}_{ik} \lambda_k + f_i \quad (49)$$

where the integrals

$$l_{ik} = \int_{\Gamma_i} Q(\mathbf{x}, \mathbf{x}_i) \psi_k(\mathbf{x}) d\Gamma_i, \quad (50)$$

$$\tilde{l}_{ik} = \int_{\Omega_i} G(\mathbf{x}, \mathbf{x}_i) \psi_k(\mathbf{x}) d\Omega_i \quad (51)$$

are calculated with the new basis $\{\psi_k\}$ instead of the Gaussian RBF basis $\{\varphi_j\}$, being Ω_i the local region of integration and Γ_i the correspondingly boundary for each ξ_i . These line and volume integrals are calculated numerically using Gauss-Legendre method of cuadrature.

Similarly to Eq. (28), here we obtained the following discretized form for the unknown field u for each internal point

$$u_i = f_i + \left(\mathbf{l}_i^T \mathbf{B}^{-1} + \tilde{\mathbf{l}}_i^T \tilde{\mathbf{B}}^{-1} \mathbf{B}_b \mathbf{B}^{-1} \right) \mathbf{d}. \quad (52)$$

with column vectors $\mathbf{l}_i = [\dots, l_{ij}, \dots]^T$ and $\tilde{\mathbf{l}}_i = [\dots, \tilde{l}_{ij}, \dots]^T$ that is solve in analogous algorithmic procedure as before.

This alternative to the LRDRM was called *Local Integral RBF-QR Method (LIM RBF-QR)* which avoid finding an auxiliary particular solution for each element of the new basis $\{\psi_k\}$ stable for small shape parameters.

4 Numerical results

In this section we explore with numerical results the stability of the RBF-QR method with integral methods and validate the formulation presented above. We consider Boundary Value Problems for different PDEs: three 2D Poisson Equations as follows, with mixed boundary conditions, with Dirichlet BC both cases in square domains and a third one over a circular domain with Dirichlet BC. Aditionally, 1D and 2D Convection-Diffusion Equations with mixed BCs. Numerical results are presented for different domains and node sets distributions uniform, halton, quasi-uniform and scattered repel distribution.

The obtained numerical results were compared with the corresponding exact solutions when available. Equations for the errors presented in this work are: *Absolute Maximum error* ($L_\infty - \text{error}$ Eq. 53), *L2 porcentual error* ($L_2 - \text{error}\%$ Eq. 54) and *Root Mean Square error* ($L_{RMS} - \text{error}$ Eq. 55).

$$L_\infty - \text{error} = \max_{i=1, \dots, N} |u_{exact}^i - u_{apx}^i| \quad (53)$$

$$L_2 - \text{error}\% = 100\% \sqrt{\frac{\sum_{i=1}^N (u_{exact}^i - u_{apx}^i)^2}{\sum_{i=1}^N (u_{exact}^i)^2}} \quad (54)$$

$$L_{RMS} - error = \sqrt{\frac{\sum_{i=1}^N (u_{exact}^i - u_{apx}^i)^2}{N}} \quad (55)$$

with u_{exact}^i as the nodal values of the exact solution and u_{apx}^i the corresponding values of the approximation. Comparisons with results in [4, 25, 26, 2] for the same equations are also reported.

4.1 Domain discretizations

The domains Ω considered in this paper were discretized using uniform and scattered nodes. For the 2D scattered nodes we used Halton [17] nodes, quasi-uniform nodes [9] and a repel algorithm presented in [2]. The construction of the first and second are based on deterministic method.

The 2-dimensional Halton nodes were created from the van der Corput sequences taking a number prime as its basis to generate well-spaced points from the interval $(0, 1)$. To generate Halton points in $(0, 1)^2$ each coordinate was generated with a different prime number. Then they were transformed linearly or translated to a rectangular domain in \mathbb{R}^2 . The boundary nodes were also generated as Halton nodes. The Matlab code used was `halton` written by B. Fornberg available at Matlab 2017a version.

The quasi-uniform nodes were created using the Matlab code `node_placing`, the implementation of a fast generation algorithm for 2D meshfree PDE discretizations developed by B. Fornberg and N. Flyer in [9]. This is an advancing front type method that creates a node set from a variable density function in rectangular and irregular domains. It starts at some boundary and advances until the total domain is filled.

The repel algorithm to create scattered nodes was described in [2]. The idea is to embed the domain Ω (a circle in our experiment) into a rectangle in 2-D and discretize it using structured nodes discarding nodes lying within certain distance to boundary. Applied a random displacement to the interior nodes in the circle and also a displacement in the direction of the repulsion force $\vec{F}(x, y) = \sum_{i=1}^n \frac{\vec{r}_i}{\|\vec{r}_i\|_2^3}$, with $\vec{r}_i = (x - x_i, y - y_i)$, n the number of closest nodes to the i -node (x_i, y_i) . The boundary $\partial\Omega$ is discretized with equispaced nodes and fixed to their position.

Uniform, Halton and quasi-uniform node distributions used in this paper for $N = 400$ and $\Omega = [-\frac{1}{2}, \frac{1}{2}] \times [-\frac{1}{2}, \frac{1}{2}]$ are shown in Fig. 5. The node distributions with more centres are similar, although denser.

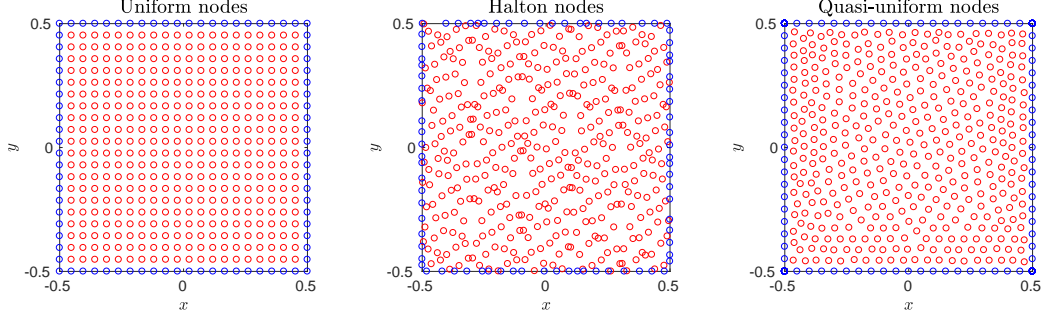


Figure 5: Discretized domain using uniform nodes. $N = 400$ interior nodes, 84 boundary nodes (left). Halton type nodes centers. $N = 400$ interior poitns, 80 boundary nodes (center). Quasi-uniform node set using $N = 401$ interior centers, 76 boundary nodes (right)

For every domain we considered a band near the boundary whereif the center node is located inside this band, the local stencil Θ_i takes n_i interior nodes and n_b boundary nodes.

All experiments were with a fixed number of nodes in the stencil except test problem 4.4 were we considered an increasing number of local stencils.

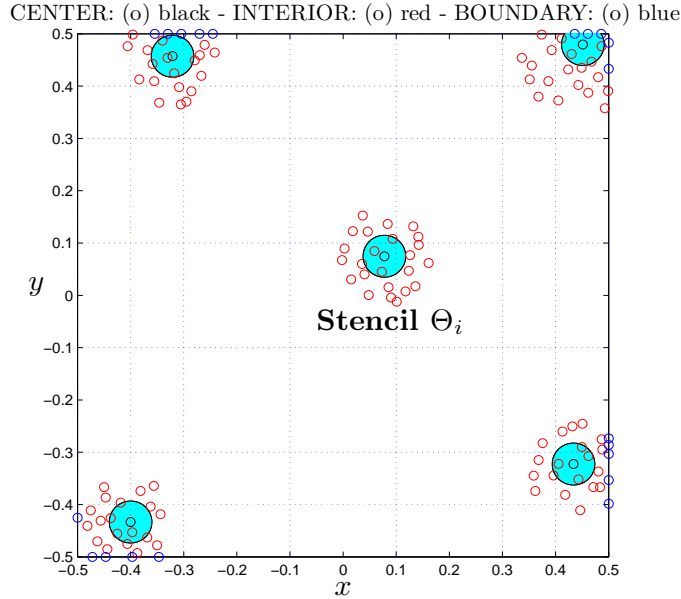


Figure 6: Stencils Θ_i and integration regions Ω_i

4.2 Poisson's equation with mixed boundary conditions

Let us consider the following elliptic PDE, a Poisson's problem whereas the non-homogenous term is a product of trigonometric functions. The governing equation in the square domain $\Omega = \left[-\frac{1}{2}, \frac{1}{2}\right]^2$ is:

$$\Delta u(x_1, x_2) = \frac{5}{4} \sin(\pi x_1) \cos\left(\frac{\pi x_2}{2}\right), \quad (x_1, x_2) \in \Omega, \quad (56)$$

and the mixed boundary conditions are:

$$(BCs) \begin{cases} u(-0.5, x_2) &= -\frac{\sqrt{2}}{2} \cos(\pi x_2), \\ u(0.5, x_2) &= \frac{\sqrt{2}}{2} \cos(\pi x_2), \\ \frac{\partial u}{\partial x_2}(x_1, -0.5) &= \pi \sin\left(\frac{\pi}{2} x_1\right), \\ \frac{\partial u}{\partial x_2}(x_1, 0.5) &= -\pi \sin\left(\frac{\pi}{2} x_1\right). \end{cases} \quad (57)$$

The analytical solution to this problem is given by $u(x_1, x_2) = \sin(\pi x_1) \cos\left(\frac{\pi x_2}{2}\right)$.

For this first example we considered uniform, Halton and quasi-uniform node set distribution, starting from a coarse distribution with $N = 400$ integration subregions, up to a denser number of subregions, $N = 2500$.

The integral equation is applied at only one source point per subdomain located at its centre with each stencil subdomain having also the same point for the local interpolation. In the numerical results in this work, N define the total number of collocation points interior of the problem domain which coincide with the number of integration subregions or Green's elements. The number of the stencil size Θ_i for the local interpolation is fixed at $n = 25$ points and the interpolation RBFs are Gaussians.

The obtained RMS error for u is reported in Fig. 7. This Figure shows the RMS error as a function of the shape parameter ε for three numerical methods. The first one is the Localized Regular Dual Reciprocity Method (LRDRM) developed in [4] using RBF GA for the local interpolation of u and the non-homogeneous term b . The second one is a modification of this method where we replaced the use of the Reciprocity method implemented before by evaluating domain integrals with Gauss-Legendre quadrature and using RBF GA basis for the local interpolation. This way of calculating the integral equations was called Localized Integral Method (LIM GA). And

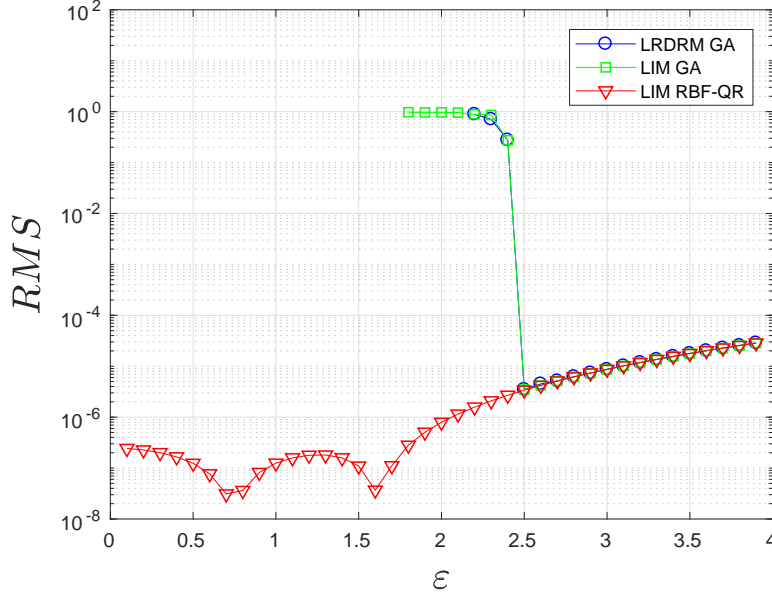


Figure 7: Comparison between LRDRM, LIM, LIM RBF-QR with Gaussians for $N = 1600$ interior points

finally, we do a further improvement for near flat RBFs using RBF-QR for the local interpolation for u and also for the term b with Gaussians RBFs.

For large ε , the three methods give the same results. The figure shows that the RMS of the LRDRM desestabilizes when the shape parameter is $\varepsilon = 2.5$ for the uniform node set distribution formed by $N = 1600$ interior nodes arriving to $3.4971E-06$ for the LRDRM and $3.4848E-06$ for LIM GA. Using the RBF-QR method locally for small shape parameters estabilizes the RMS method significantly. The RMS in this case is $3.1063E-08$, 2 orders of magnitude better. The uniform discretizations for $N = 400, 900, 2500$ have the same behavior arriving to $1,8359E-07$, $5,8726E-08$ and $2.0682E-08$ respectively. The total comparison is shown in Table 2 for the uniform distribution.

N	LRDRM GA		LIM GA		LIM RBF-QR (1st dip)		LIM RBF-QR (2nd dip)	
	ϵ	RMS	ϵ	RMS	ϵ	RMS	ϵ	RMS
400	1.60	1.1460E-06	1.60	1.1208E-06	1.60	1.1174E-06	0.80	1.8359E-07
900	1.90	1.6175E-06	1.90	1.6082E-06	1.60	1.5320E-07	0.80	5.8726E-08
1600	2.50	3.4971E-06	2.50	3.4849E-06	1.60	3.6854E-08	0.70	3.1063E-08
2500	2.90	4.1908E-06	2.90	4.3092E-06	1.60	2.3318E-08	0.70	2.0682E-08

Table 2: Poisson PDE with mixed BC - RMS - Uniform distribution

Fig. 8 shows the RMS versus the shape parameter for the different uniform distributions when $\varepsilon \rightarrow 0$. It is known that decreasing the shape parameter ε produce more flat RBFs Gaussians which allow more accuracy in the numerical solution of the two systems for the local interpolation matrix \mathbf{A} and $\tilde{\mathbf{A}}$. This ill conditioning dominates the error of the Local Integral Method. It is observed also that the error due to Runge phenomenon emerges. Such is the case in Fig. 8, where we show for different node sets. This error reaches very low levels but for values near $\varepsilon = 0.8$ and $\varepsilon = 1.6$ increases. When increasing the number of total nodes, the difference between the first dip and the second becomes smaller (column 3rd and 4th from Table). This is due to the Runge phenomenon studied in [15] since no particular mechanism was taken for controlling that. Note that for the uniform nodes distribution the location of these *curve dips* not depends on the number of points N since they appear for the same ε s. An advanced strategy for dealing with the Runge phenomenon is to use *spatially varying* shape parameters like in [15].

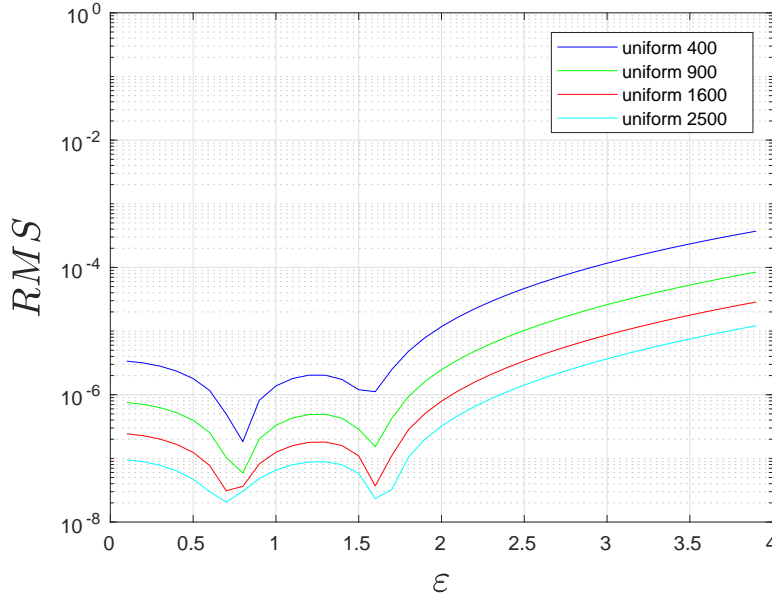


Figure 8: Runge phenomenon in the RMS error comparison between different uniform node sets for the Local Integral RBF-QR Method for $\varepsilon \in [0.1, 4.0]$.

Fig. 9 shows numerical experiments for the RMS error of the LIM RBF-QR for the uniform, Halton and quasi-uniform node sets distributions, with

total number of interior points $N = 400, 900, 1600, 2500$ in each subfigure. In all cases, we see that the best accuracy of the numerical solution is obtained for the smaller values of ε and also, we increase the number of total collocation points. The method LIM RBF-QR with the uniform distribution shows the Runge phenomenon explained above as in Fig. 8. For cases of halton points and quasi-uniform points, we see that the major change in the trend of $\varepsilon \rightarrow 0$ when the number of collocation points is increase from $N = 900$ to $N = 2500$. For $N = 1600$, we see that the halton distribution follows the same pattern of the Runge phenomenon as in the uniform case, while the quasi-uniform distribution stabilizes for $\varepsilon < 2$ and continues decreasing as $\varepsilon \rightarrow 0$. In the case $N = 2500$, we see that the halton distribution stabilizes around $\varepsilon < 1.3$ while the quasi-uniform distribution around $\varepsilon < 1.7$. This results are the expected for small ε 's since the RBF-QR was originally implemented for small values.

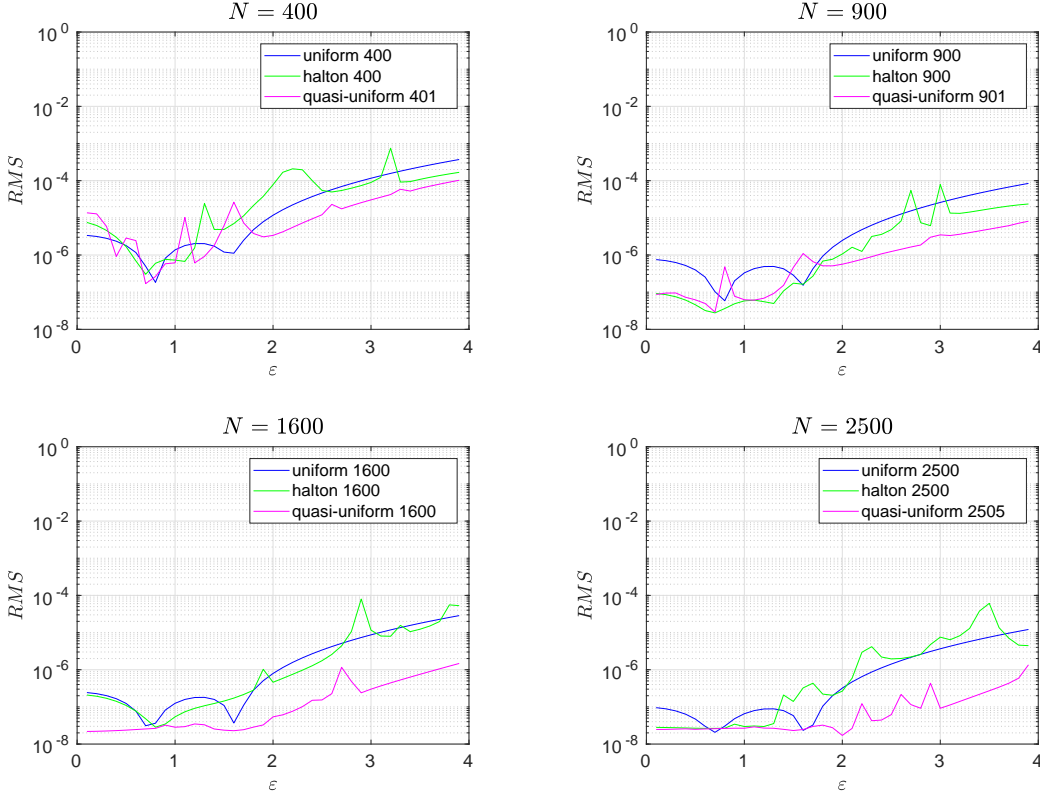


Figure 9: Comparison for uniform, halton and quasi-uniform node sets distributions for $N = 400$ (left) and $N = 2500$ (right) interior nodes.

All these results are due to the severe dependence of the conditioning of the interpolation matrix for the local interpolation for u and b of the shape parameter ε . As it was study in [15], for a constant shape parameter, the interpolation matrix \mathbf{A} of a 2-D non-periodic distribution of points for IQ, MQ or GA RBF is:

$$\text{cond}(\mathbf{A}) = O\left(\frac{1}{\varepsilon^{2[\sqrt{8n-7}-1]}}\right). \quad (58)$$

where $[\cdot]$ denotes the integer part and n the points of the local interpolation. So for the Halton and quasi-uniform distributions we have $\text{cond}(A) = O(\varepsilon^{-12})$. Solving the local linear systems of equations for the ill-conditioned interpolation matrix (12) and (7) with a direct method (RBF-Direct) give worst results that making the change of basis proposed in the RBF-Qr method.

4.3 Poisson's equation with Dirichlet boundary conditions

Let's consider the following Poisson's equation defined in the domain $\Omega = [1, 2]^2$:

$$\begin{aligned} \Delta u(x, y) = & - \frac{751}{144} \pi^2 \sin\left(\frac{\pi}{6}x\right) \sin\left(\frac{7}{4}\pi x\right) \sin\left(\frac{3}{4}\pi y\right) \sin\left(\frac{5}{4}\pi y\right) \\ & + \frac{7}{12} \pi^2 \cos\left(\frac{\pi}{6}x\right) \cos\left(\frac{7}{4}\pi x\right) \sin\left(\frac{3}{4}\pi y\right) \sin\left(\frac{5}{4}\pi y\right) \\ & + \frac{15}{8} \pi^2 \sin\left(\frac{\pi}{6}x\right) \sin\left(\frac{7}{4}\pi x\right) \cos\left(\frac{3}{4}\pi y\right) \cos\left(\frac{5}{4}\pi y\right) \end{aligned} \quad (59)$$

with Dirichlet boundary conditions:

$$(BCs) \begin{cases} u(x, 1) &= -\frac{1}{2} \sin\left(\frac{\pi}{6}x\right) \sin\left(\frac{7\pi}{4}x\right), \\ u(x, 2) &= -\sin\left(\frac{\pi}{6}x\right) \sin\left(\frac{7}{4}y\right), \\ u(1, y) &= -\frac{1}{2\sqrt{2}} \sin\left(\frac{3\pi}{4}y\right) \sin\left(\frac{5\pi}{4}y\right), \\ u(2, y) &= \frac{3}{\sqrt{2}} \sin\left(\frac{3\pi}{4}y\right) \sin\left(\frac{5\pi}{4}y\right). \end{cases} \quad (60)$$

The analytical solution to this problem is: $u(x, y) = \sin\left(\frac{\pi}{6}x\right) \sin\left(\frac{7}{4}\pi x\right) \sin\left(\frac{3}{4}\pi y\right) \sin\left(\frac{5}{4}\pi y\right)$.

As in the numerical experiment before, the node set distributions implemented were uniform, Halton and quasi-uniform for $N = 400, 900, 1600, 2500$

interior points, $N_b = 84, 124, 164, 204$ boundary points and $n = 25$ points for the local stencils Θ_i .

The objective in solving this PDE was to compare numerical results of three different local integral methods reported in the literature, the results obtained with the LRDRM in [4], those found by Ooi and Popov [25] using the Radial Basis Integral Equation Method (RIBEM) and finally the LIM RBF-QR presented in this paper.

For the uniform case, the convergence analysis through the L_2 error norm is presented in Fig. 10 and 11 for u . Comparison between the numerical results obtained with the LRDRM and the RIBEM, [25], are also presented in Fig. 10, where as before it can be seen that the LIM RBF-QR results are more accurate than those obtained with the LRDRM and RIBEM by one or two order of magnitude or more. For $N = 6400$ the RIBEM achieved the $L_2 - error\%$ of $8.000E-03$ and the LRDRM $6.5021E-04$. The best results for this PDE were obtained with LIM RBF-QR were the errors varies from $2.4698E-04$, $3.75833E-05$, $1.2626E-05$, $8.4696E-06$, $6.2864E-06$ for $N = 400, 900, 1600, 2500, 3600$ respectively.

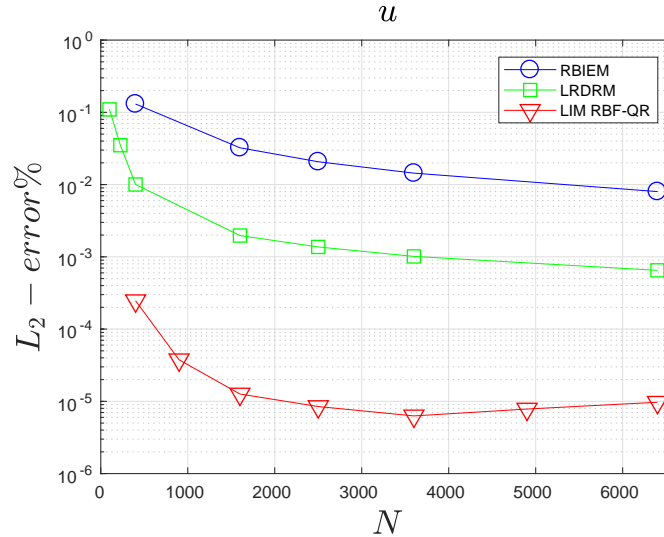


Figure 10: Comparison of the $L_2 - error\%$ between RIBEM, LRDRM and LIM RBF-QR for uniform node set. N number of interior nodes of the domain.

In Fig. 11 we compare the $L_2 - error\%$ versus the number of interior points for the different types of distribution node sets. As expected, all the

schemes show that the stability with RBF-QR for the local interpolation matrix of the unknown field u and the non-homogeneous term b gave the best numerical results, that we call LIM RBF-QR. As in this case b depends just on the variable \mathbf{x} , it was integrated in two different ways. The first one was to considered the integral over the domain Ω_i like in Eq. (24) being $b_2 = 0$ (that was called LIM Sint GA). And the second one, was to considered b as a linear combination of Gaussians RBFs Eq. (7)) and then interpolated (called LIM Sapprox GA). This numerical modification gave no numerical difference in orders of magnitude of the error.

This two alternatives of integrating b had a better behavior for the quasi-uniform distribution arriving to values of the $L_2 - error\%$ as low as 7.9410E-05 and 7.9549E-05 respectively for $N = 1600$. In the uniform case, the $L_2 - error\%$ achieve 2.2318E-04 and 2.2530E-04 for $N = 900$. For the LIM RBF-QR the best behavior is obtained with uniform and quasi-uniform points achieving 8.4696E-06 in the uniform case for $N = 2500$ and 1.5995E-05 in the quasi-uniform case for $N = 2505$.

The Halton case does not show uniform convergence for all the methods.

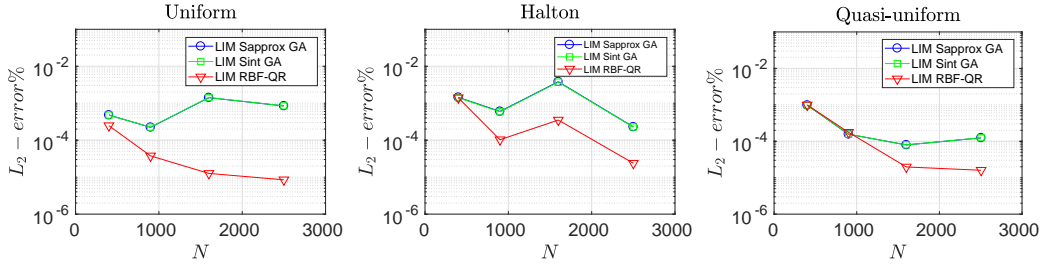


Figure 11: $L_2 - error\%$ versus N for uniform, Halton and quasi-uniform distributions

4.4 Poisson's equation over the unit disk

The final Poisson's equation with Dirichlet boundary conditions is defined over the circular domain $\Omega = \{(x, y)/x^2 + y^2 \leq 1\}$:

$$\begin{cases} \Delta u = -200 \sin[10(x + y)] & (x, y) \in \Omega, \\ u = \sin[10(x + y)] & (x, y) \in \partial\Omega \text{ (BCs)}. \end{cases} \quad (61)$$

The exact solution to this problem is plotted in Fig. 12 and is given by: $u(x, y) = \sin[10(x + y)]$.

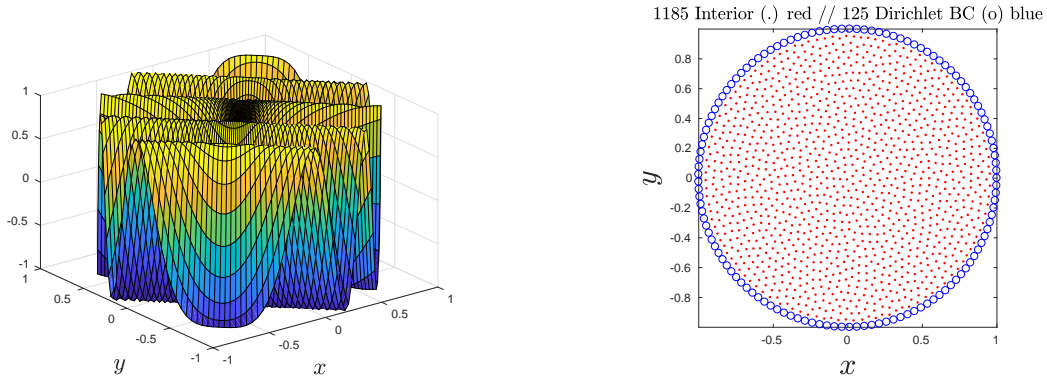


Figure 12: Exact solution (left) and quasi-uniform point distribution (right)

The results are compared with those found by Bayona et al [2] using RBF-Generatad Finite Difference method with polynomial augmentation. This method is a combination of polyharmonic splines (PHS) with multivalue polynomials for solving PDEs that has emerge in the last decade as a powerful and flexible numerical approach. In that paper, several strategies were used to avoid the accuracy and stability problems of using one-side stencils near boundaries for elliptic PDEs. Besides, our objective in this experiment is to compare integral and difference numerical method that use near flat RBF without any treatment at the boundaries and also using the RBF-QR method to stabilize the local interpolation errors.

The present scattered nodes distribution to experiment was formed by $N = 1185$, 4880 interior nodes and $N_b = 125$, 251 boundary nodes respectively. Fig. 12 (right) shows the nodes distribution for $h = 0.025$ ($N = 1185$ interior nodes), where the structure for $h = 0.01$ ($N = 4880$ interior nodes) is similar, but denser. The left figure shows the oscillatory behavior of the analytical solution over the unit disk.

Fig. 13 shows the isolines order $L_2 - error$ as a function of the stencil size and the shape parameter for the different node sets (row subplots) and local integral numerical methods with/without RBF-QR (column subplots). Without any special treatment of the boundary, the interior nodes are used as collocation nodes obtaining a one side stencils near the boundary. The number of points for local stencils varies from $n = 10$ to $n = 100$.

The first observation is that the error decreases as the node distribution is refined from $N = 1185$ to $N = 4880$ and also when the shape parameter ε tends to zero in the four subplots. The introduction of the RBF-QR method

in the local interpolation of the integral methods produces the same effects than in the Poisson equations before. Decreasing the shape parameter of the Gaussian RBF for the local interpolation, improved the accuracy of the LIM until the breakdown error occurs.

In the first column of subplots we show a wide region of inestability for $N = 1185$ that began for $\varepsilon < 4$ and $n > 30$ to the left and up. The best order error is 10^{-5} obtained in two peaks bewteen $3 < \varepsilon < 3.6$ and $65 < n < 70$ and $4 < \varepsilon < 4.5$ and $85 < n < 100$. Also for $N = 4880$ this inestability's region began from $\varepsilon < 8$ and $n > 20$ to left and up. This is because the near flat Gaussians RBFs produce ill-conditioned matrix for the local interpolation matrices that increases their size so the direct local solver increases the local error. Is is expectable that increasing the number of points in the local stencils, the accuracy of the LRDIM decreases. The best order error is 10^{-5} from $3 < \varepsilon < 5.6$ and $20 < n < 40$ and there is another region of the same order for $6 < \varepsilon < 9.8$ and $45 < n < 100$.

The second column shows the effects of the RBF-QR. The inestability region expands from $1.5 < \varepsilon < 4.2$ and $63 < n < 100$ for order 10^{-5} at the case $N = 1185$, and from $1 < \varepsilon < 7$ and $35 < n < 100$ for order 10^{-6} in the case $N = 4880$.

4.5 One-dimensional Convection-Diffusion equation

To test the performance of the proposed LIM RBF-QR on differential problems that comes from applications, we consider a steady state convection-diffusion equation with a variable velocity field that has been used before as test example of different implementations in the literature [27, 30]

$$D \frac{\partial^2 u(\mathbf{x})}{\partial x_i^2} - V_{x_1} \frac{\partial u(\mathbf{x})}{\partial x_1} - k u(\mathbf{x}) = 0 \quad (62)$$

with convective velocity field

$$V_{x_1} = \ln \frac{U_1}{U_0} + k \left(x_1 - \frac{1}{2} \right); \quad V_{x_2} = 0 \quad (63)$$

corresponding to the flow of a hypothetical compressible fluid with a density variation inversely proportional to the velocity field.

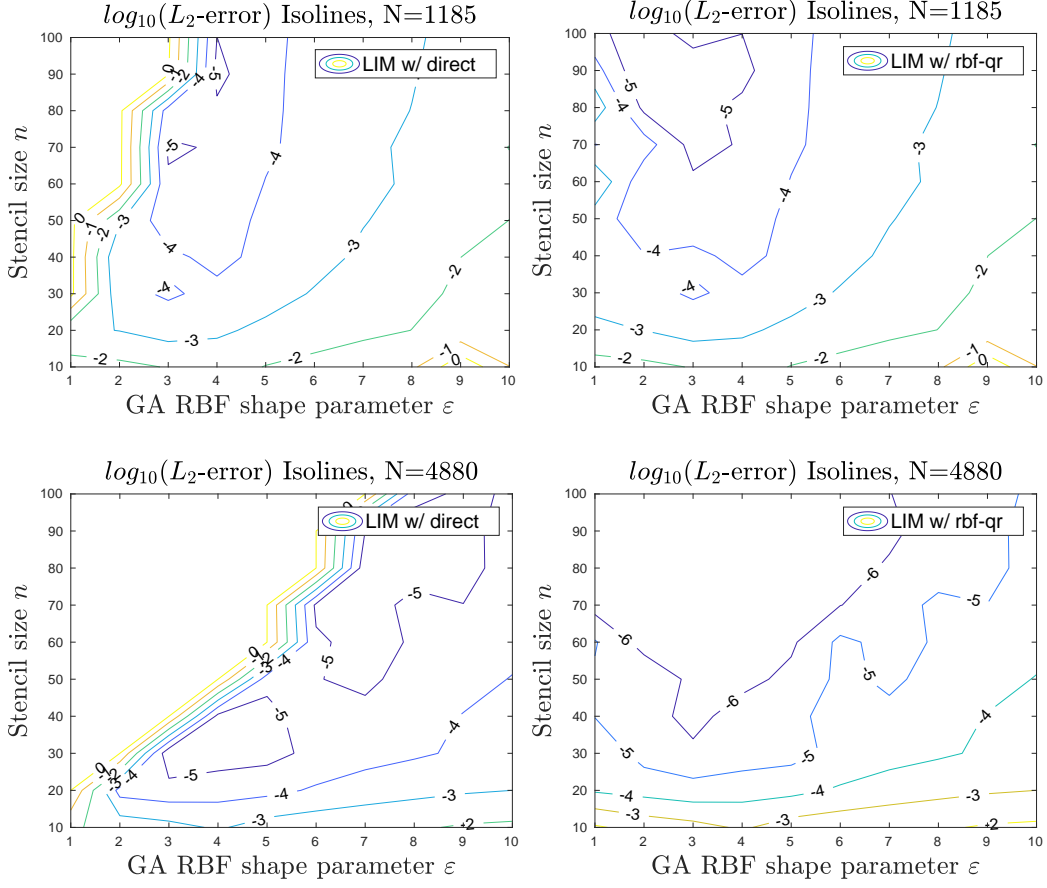


Figure 13: Accuracy ($\log_{10}(L_2 - \text{error})$) isolines) when using RBF GA as a function of the stencil size and shape parameter for quasi-uniform distribution for $N = 1185$ and $N = 4880$ with and without RBF-QR.

The analytical solution of the above boundary value problem for a diffusion coefficient $D = 1$ is given by

$$u(\mathbf{x}) = U_0 \exp \left\{ \frac{k}{2} x_1^2 + \left(\ln \frac{U_1}{U_0} - \frac{k}{2} \right) x_1 \right\} \quad (64)$$

showing the formation of shock structures at each side of the problem domain. To analyse the performance of the numerical scheme different values of the decay parameter k in the convective velocity are considered, where larger values of k correspond to stronger shock structures at the problem boundaries.

For the numerical solution, this 1-D problem is considered as a 2-D one in a rectangular domain $\Omega = [0, 1] \times [-0.1, 0.1]$ subject to the following boundary conditions

$$\begin{cases} u(0, x_2) = U_0, & u(1, x_2) = U_1, \\ \frac{\partial u}{\partial x_2}(x_1, -0.1) = 0, & \frac{\partial u}{\partial x_2}(x_1, 0.1) = 0, \end{cases} \quad (65)$$

where the domain Ω is subdivided into subdomains Ω_i that are used to construct the interpolation stencils Θ_i . The distribution node sets considered were uniform, Halton and quasi-uniform. See Table 3.

Uniform			Halton			Quasi-uniform		
N	N_{Dir}	N_{Neu}	N	N_{Dir}	N_{Neu}	N	N_{Dir}	N_{Neu}
500	100	24	500	100	20	500	100	22
1125	150	34	1125	150	30	1127	150	32
2000	200	44	2000	200	40	1981	198	42
3125	250	54	3125	250	50	3125	250	52
4500	300	64	4500	300	60	4501	300	62
6125	350	74	6125	350	70	6158	352	74
8000	400	84	8000	400	80	7987	404	84

Table 3: Number of discretizations

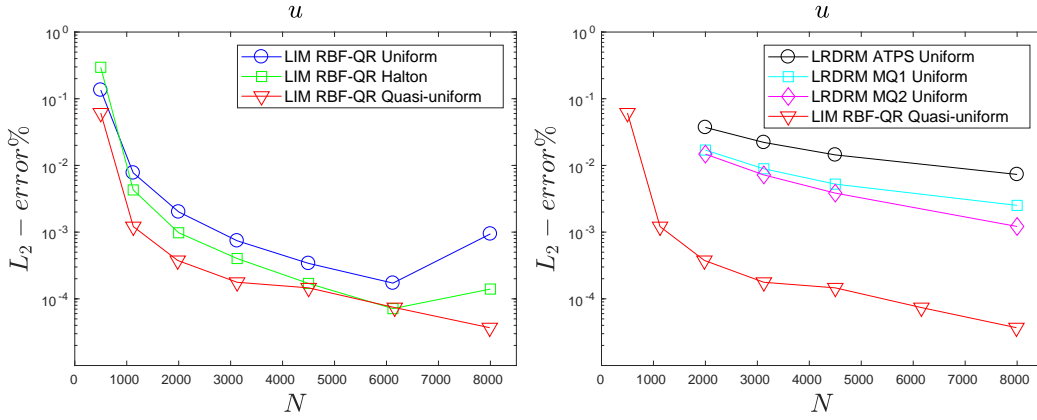


Figure 14: Comparison between different methods $k = 40$

The difference between the LIM RBF-QR and LRDRM presented in [4] are shown in Fig. 14 (left). It can be seen that for $k = 40$, the best $L_2 - Error\%$ is obtained for the LIM RBF-QR over the quasi-uniform points,

that is using locally RBF-QR method to achieve low errors with small shape parameters. In this case the integral equation is applied at only one collocation point per subdomain located at its centre with each stencil subdomain having $n = 25$ points every stencil. With this 25-points stencils for the quasi-uniform distribution the values of the $L_2 - Error\%$ is as low as $3.6878E - 05$ for u . In Table 4 we show the comparison for the different distributions and different values of k . It is observed that the results for the LRDRM where obtained with $N = 20480$ uniform interior nodes, but in the case $k = 40$ and $k = 100$ for the LIM RBF-QR we need less points to achieve one order of magnitude less. For the case $k = 200$ we achieved the same order that the LRDRM with $N = 20480$ interior points but with $N = 8000, 6125, 7987$ for the distributions uniform, halton and quasi-uniform respectely. The LIM RBF-QR for $N = 7987$ quasi-uniform nodes achieved $1.6580E - 02$ lower that $3.4485E - 02$ for $N = 20480$ for uniform points.

Also, if we compare the different distributions we observed that the best result was obtained for the quasi-uniform points. See Fig 14 (right). For $k = 40$ with the LIM RBF-QR the uniform and Halton nodes set distribution the $L_2 - Error\%$ versus the number of interior points decreases from $N = 500$ to $N = 6125$ achieving the best errors values of $1.7186E - 04$ and $7.1334E - 05$ for $N = 6125$. While for the quasi-uniform, the error continue decreasing until $3.6878E - 05$ for $N = 7987$ points.

	LRDRM		LIM RBF-QR					
	Uniform		Uniform		Halton		Quasi-uniform	
k	N	$L_2 - error\%$	N	$L_2 - error\%$	N	$L_2 - error\%$	N	$L_2 - error\%$
40	20480	6.83E-04	6125	1.7186E-04	6125	7.1334E-05	7987	3.6878E-05
100	20480	4.32E-03	6125	1.1654E-04	6125	2.8154E-03	7987	5.8630E-04
200	20480	3.44E-02	8000	6.2399E-02	6125	8.7114E-02	7987	1.6580E-02

Table 4: **CDRE 1D** - For different k - $L_2 - error\%$

4.6 Thermal boundary layer in a two dimensional channel

As a final example, let us consider a 2D steady state flow entering a parallel channel with different walls temperatures. The governing equation is

$$\Delta T(x_1, x_2) - PeV(x_2) \frac{\partial T}{\partial x_1} = 0 \quad (66)$$

where the parabolic velocity distribution is $V(x_2) = 4x_2(x_2 - 1)$ and Pe is the Péclet number. The computational domain is taken to be $\Omega = [0, 1]^2$ and the following Dirichlet and Neumann boundary conditions are imposed:

$$\left\{ \begin{array}{lll} T(x_1, 0) & = & 1 \quad 0 \leq x_1 \leq 1 \\ T(x_1, 1) & = & 0 \quad 0 \leq x_1 \leq 1 \\ T(0, x_2) & = & 0 \quad 0 \leq x_2 \leq 1 \\ \frac{\partial T}{\partial x_1}(1, x_2) & = & 0 \quad 0 \leq x_2 \leq 1 \end{array} \right. \quad (67)$$

There is no analytical solution for this PDE.

The objective in this example was to obtain numerical solutions in low values of the shape parameter ε for different quasi-uniform node sets and three different values of global Peclet number Pe . Fig. 15 show results for $Pe = 0.25$, Fig.16 for $Pe = 50$ and Fig. 17 for $Pe = 125$. In all Figures we show from left to right the approximated solution, the x_1 and x_2 sections in that order. For the reconstruction of the solution we use Biharmonic spline interpolation that is an interpolation of the irregular 2D data points that we obtain from the integral method. This interpolating surface is a linear combination of Green functions centered at each data point. For more references see [32, 6].

For all the values of the Peclet numbers studied with LIM RBF-QR, the obtained numerical results were numerically stable without oscillations for low levels of ε . In the Figures we show that to achieve $\varepsilon = 0.1$ we need $N = 901$ quasi-uniform points for the PDE with $Pe = 0.25$ and $Pe = 50$. For the global Peclet $Pe = 125$ we need $N = 2505$ interior points.

When we considered the LIM without RBF-QR and with GA RBFs for local interpolations for u and b , we obtained that for shape parameters $\varepsilon < 1$, the numerical approximation presented several oscillations in all cases. This is because the condition number of the RBF local interpolation matrix varies between 10^{17} and 10^{21} .

5 Conclusions

In this paper, a method based on a local integral approach considering local RBF interpolation has been presented with the improvement of the numerical technique RBF-QR to achieve good results for low range of the shape parameter. This method was called the LIM RBF-QR. The robustness of this numerical method has been assessed for several elliptic PDEs with

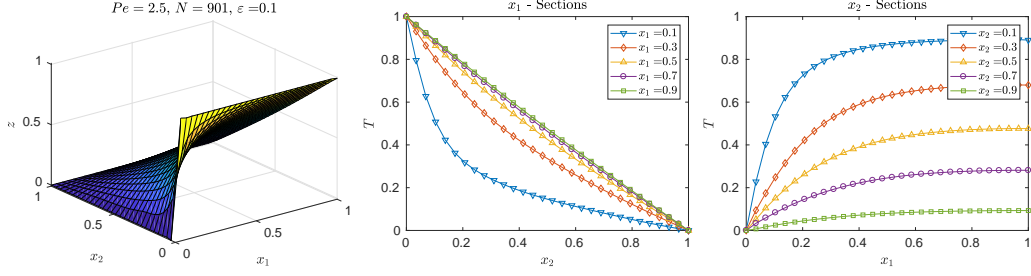


Figure 15: LIM RBF-QR - Quasi-uniform point distribution - $Pe = 2.5$ - $N = 901$ - $\varepsilon = 0.1$

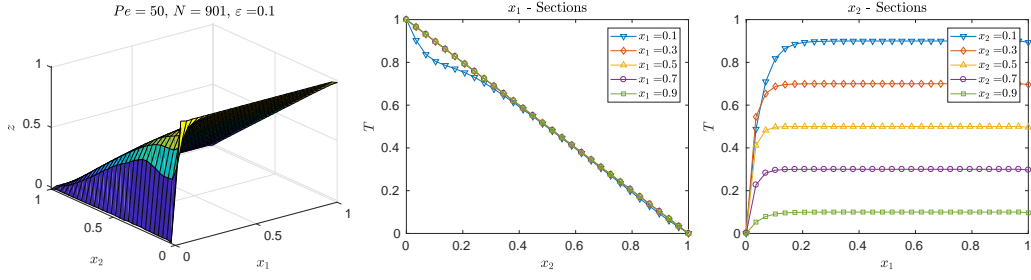


Figure 16: LIM RBF-QR - Quasi-uniform point distribution - $Pe = 50$ - $N = 901$ - $\varepsilon = 0.1$

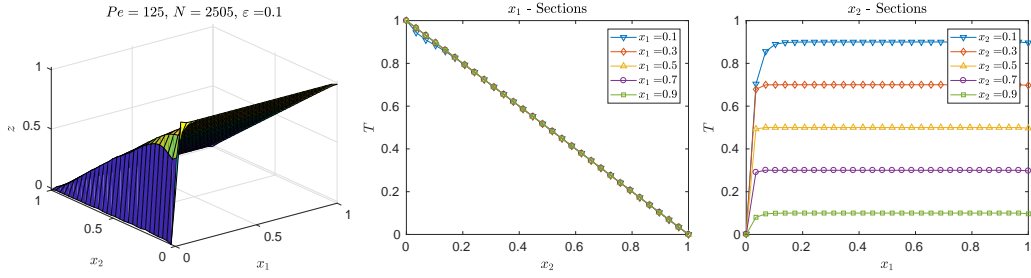


Figure 17: LIM RBF-QR - Quasi-uniform point distribution - $Pe = 125$ - $N = 2505$ - $\varepsilon = 0.1$

Dirichlet and Neumann BC over different domains and with scattered distributions as Halton or quasi-uniform points. For a Poisson equation with mixed BC over a square using LIM RBF-QR we improve the *RMS* error one order of magnitude of the LRDRM with Gaussians RBF for $N = 400$ uniform points. We also improved two order for $N = 900, 1600, 2500$ with $\varepsilon < 1$. For a Poisson problem with Dirichlet BC we improve with

$\varepsilon = 1.4$ by three orders the results presented for the RBIEM with TPS and one order for LRDRM with MQ2 for $N = 400$ interior points. For $N = 900, 1600, 2500, 3600, 4900, 6400$ the improvement was by three and two orders respectively using $\varepsilon = 1.4, 1.3, 1.1, 0.2, 0.1, 0.1$ respectively. For the Poisson problem over the unit disk with the RBF-QR scheme, a larger region of convergence with $N = 1185$ centres is observed for L_2 -error of orders 10^{-3} , 10^{-4} and 10^{-5} (with smaller values of the shape parameter and greater number of points per stencil) to the obtained with Direct LIM with Gaussians RBF. In the case of $N = 4880$ interior centres, the region of convergence obtained of orders 10^{-3} , 10^{-4} and 10^{-5} are larger and also we achieved to a region of order 10^{-6} for small ε and stencil size bigger than $n = 40$ points. All these results improved the numerical L_2 -errors presented using RBF-Generated Finite Difference method with polynomial augmentation for the same problem. For the Convection-Diffusion PDE, the $L_2\%$ error for the discretization tested was improved by two orders of magnitude. Even better order of magnitude results are obtained for LIM RBF-QR with a discretization of $N = 1127$ quasi-uniform points, with respect to results of LRDRM for $N = 8000$ uniform points with TPS, MQ1 and MQ2. For the Thermal Boundary Layer PDE (numerically unstable from $Pe = 2$ and without analytical solution), using LIM RBF-QR with $\varepsilon = 0.1$ we obtained good results for the reconstruction with biharmonic splines of the numerical approximation for Péclet 2.5, 50 and 125 values.

6 Acknowledgments

The authors would like to thank Elisabeth Larsson from Uppsala University for the collaboration on the RBF-QR implementation method, and Bengt Fornberg from University of Colorado at Boulder and Natasha Flyer from the National Center for Atmospheric Research (NCAR) at Boulder, CO, US for their valuable discussions and suggestions provided. We also acknowledge the contributions of Professor Henry Power (1950-2017) from University of Nottingham in memoriam.

References

- [1] S. N. Atluri and T. Zhu. New meshless local petrov-galerkin (MLPG) approach in computational mechanics. *Computational Mechanics*, 22(2):117–127, 1998.
- [2] V. Bayona, N. Flyer, B. Fornberg, and G. Barnett. On the role of polynomials in RBF-FD approximations: II. Numerical solution of elliptic PDEs. *Journal of Computational Physics*, 332:257–273, 2017.
- [3] M. Buhmann and N. Dyn. Spectral convergence of multiquadric interpolation. *Proceedings of the Edinburgh Mathematical Society*, 36(2):319–333, 1993.
- [4] N. Caruso, M. Portapila, and H. Power. An efficient and accurate implementation of the localized regular dual reciprocity method (LRDRM). *Computers and Mathematics with Applications*, 69:1342–1366, 2015.
- [5] N. Caruso, M. Portapila, and H. Power. PDE centres enhancement in the localized regular dual reciprocity method. *Engineering Analysis with Boundary Elements*, 64:255–266, 2016.
- [6] X. Deng and Z. Tang. Moving surface spline interpolation based on green’s function. *Mathematical Geosciences*, 43:663–680, 2011.
- [7] G. Faashauer and M. McCourt. *Kernel-based Approximation Methods using MATLAB*. World Scientific Publishing Co., Hackensack, NJ, USA, 2015.
- [8] G. Fasshauer. *Meshfree Approximation Methods with MATLAB*. World Scientific Publishing Co., Hackensack, NJ, USA, 2007.
- [9] B. Fornberg and N. Flyer. Fast generation of 2-D node distributions for mesh-free pde discretizations. *Computers and Mathematics with Applications*, 69:531–544, 2015.
- [10] B. Fornberg and N. Flyer. *A Primer on Radial Basis Functions with Applications to the Geosciences*. Society for Industrial and Applied Mathematics, Philadelphia, PA, USA, 2015.

- [11] B. Fornberg, E. Larsson, and N. Flyer. Stable computation with gaussian radial basis functions. *SIAM Journal of Scientific Computing*, 33(2):869–892, 2011.
- [12] B. Fornberg, E. Lehto, and C. Powell. Stable calculation of gaussian-based RBF-FD stencils. *Computers and Mathematics with Applications*, 65:627–637, 2013.
- [13] B. Fornberg and C. Piret. A stable algorithm for flat radial basis functions on a sphere. *SIAM Journal of Scientific Computing*, 30:60–80, 2007.
- [14] B. Fornberg and G. Wright. Stable computation of multiquadric interpolations for all values of the shape parameter. *Computers and Mathematics with Applications*, 48:853–867, 2004.
- [15] B. Fornberg and J. Zuev. The Runge phenomenon and spatially variable shape parameters in rbf interpolation. *Computers and Mathematics with Applications*, 54(3):379–398, 2007.
- [16] S. Güttel and J. Pestana. Some observations on weighted gmres. *Numerical Algorithms*, pages 1–20, 2014.
- [17] J. Halton. On the efficiency of certain quasi-random sequences of points in evaluating multi-dimensional integrals. *Numerische Mathematik*, 2:84–90, 1960.
- [18] E. Larsson and B. Fornberg. A numerical study of some radial basis function based solution methods for elliptic PDEs. *Computers and Mathematics with Applications*, 46:891–902, 2003.
- [19] E. Larsson and B. Fornberg. Theoretical and computational aspects of multivariate interpolation with increasingly flat radial basis functions. *Computers and Mathematics with Applications*, 49:103–130, 2005.
- [20] E. Larsson, E. Lehto, A. Heryudono, and B. Fornberg. Stable computation of differentiation matrices and scattered node stencils on gaussian radial basis functions. *SIAM Journal of Scientific Computing*, 35(4):A2096–A2119, 2013.

- [21] W. R. Madych and S. A. Nelson. Bounds on multivariate polynomials and exponential error estimates for multiquadric interpolation. *Journal of Approximation Theory*, 70:94–114, 1992.
- [22] C. Micchelli. Interpolation of scattered data: Distance matrices and conditionally positive definite functions. *Constructive Approximation*, 2(1):11–22, 1986.
- [23] L. Milne-Thomson. *Theoretical Hydrodynamics*. The Macmillan Company, New York, 1968.
- [24] D. Nardini and C. A. Brebbia. Boundary element integral formulation of mass matrices for dynamic analysis (Chapter 7). In C. A. Brebbia, editor, *Topics in Boundary Elements Research*, pages 191–207. Springer-Verlag, Berlin and New York, 1985.
- [25] E. H. Ooi and V. Popov. An efficient implementation of the radial basis integral equation method. *Engineering Analysis with Boundary Elements*, 36:716–726, 2012.
- [26] E. H. Ooi and V. Popov. A simplified approach for imposing the boundary conditions in the local boundary integral equation method. *Computational Mechanics*, 51(5):717–729, 2013.
- [27] V. Popov and T. T. Bui. A meshless solution to two-dimensional convection-diffusion problems. *Engineering Analysis with Boundary Elements*, 34:680–689, 2010.
- [28] V. Popov and H. Power. The DRM-MD integral equation method: an efficient approach for the numerical solution of domain dominant problems. *International Journal for Numerical Methods in Engineering*, 44(3):327–353, 1999.
- [29] M. Portapila and H. Power. A convergence analysis of the performance of the DRM-MD boundary integral approach. *International Journal for Numerical Methods in Engineering*, 71:47–65, 2007.
- [30] M. Portapila and H. Power. Iterative solution schemes for quadratic DRM-MD. *Numerical Methods for Partial Differential Equations*, 24(6):1430–1459, 2008.

- [31] H. Power, N. Caruso, and M. Portapila. A note on the use of the companion solution (Dirichlet Green's function) on meshless boundary element methods. *Engineering Analysis with Boundary Elements*, 75:57–64, 2017.
- [32] D. Sandwell. Biharmonic spline interpolation of GEOS-3 and SEASAT altimeter data. *Geophysics Research Letters*, 14:139–142, 1987.
- [33] R. Schaback. Error estimates and condition numbers for radial basis function interpolatns. *Advances in Computational Mathematics*, 3:251–264, 1995.
- [34] E. J. Sellountos, D. Polyzos, and S. N. Atluri. A new and simple meshless lbie-rbf numerical scheme in linear elasticit. *Computer Modeling in Engineering adn Sciences*, 89(6):513–551, 2012.
- [35] J. Sladek, V. Sladek, and C. Zhang. A local biem for analysis of transient heat conduction with nonlinear source terms in fgms. *Engineering Analysis with Boundary Elements*, 28:1–11, 2004.
- [36] T. Zhu, J. D. Zhang, and S. N. Atluri. A local boundary integral equation (LBIE) method in computational mechanics, and a meshless discretization approach. *Computational Mechanics*, 21:223–235, 1998.